A novel anisotropic inversion approach for magnetotelluric data from subsurfaces with orthogonal geoelectric strike directions

Jan-Philipp Schmoldt[1,2] and Alan G. Jones[1]

[1]*School of Cosmic Physics, Dublin Institute for Advanced Studies, Dublin* 2, *Ireland. E-mail: janschmoldt@gmail.com*
[2]*National University of Ireland, Galway, University Road, Galway, Ireland*

SUMMARY

The key result of this study is the development of a novel inversion approach for cases of orthogonal, or close to orthogonal, geoelectric strike directions at different depth ranges, for example, crustal and mantle depths. Oblique geoelectric strike directions are a well-known issue in commonly employed isotropic 2-D inversion of MT data. Whereas recovery of upper (crustal) structures can, in most cases, be achieved in a straightforward manner, deriving lower (mantle) structures is more challenging with isotropic 2-D inversion in the case of an overlying region (crust) with different geoelectric strike direction. Thus, investigators may resort to computationally expensive and more limited 3-D inversion in order to derive the electric resistivity distribution at mantle depths. In the novel approaches presented in this paper, electric anisotropy is used to image 2-D structures in one depth range, whereas the other region is modelled with an isotropic 1-D or 2-D approach, as a result significantly reducing computational costs of the inversion in comparison with 3-D inversion. The 1- and 2-D versions of the novel approach were tested using a synthetic 3-D subsurface model with orthogonal strike directions at crust and mantle depths and their performance was compared to results of isotropic 2-D inversion. Structures at crustal depths were reasonably well recovered by all inversion approaches, whereas recovery of mantle structures varied significantly between the different approaches. Isotropic 2-D inversion models, despite decomposition of the electric impedance tensor and using a wide range of inversion parameters, exhibited severe artefacts thereby confirming the requirement of either an enhanced or a higher dimensionality inversion approach. With the anisotropic 1-D inversion approach, mantle structures of the synthetic model were recovered reasonably well with anisotropy values parallel to the mantle strike direction (in this study anisotropy was assigned to the mantle region), indicating applicability of the novel approach for basic subsurface cases. For the more complex subsurface cases, however, the anisotropic 1-D inversion approach is likely to yield implausible models of the electric resistivity distribution due to inapplicability of the 1-D approximation. Owing to the higher number of degrees of freedom, the anisotropic 2-D inversion approach can cope with more complex subsurface cases and is the recommended tool for real data sets recorded in regions with orthogonal geoelectric strike directions.

Key words: Inverse theory; Numerical approximations and analysis; Electromagnetic theory; Magnetotelluric.

1 INTRODUCTION

2-D inversion of magnetotelluric (MT) data is, at present, far more commonly used than 3-D inversion, since 2-D inversion significantly outperforms 3-D inversion in terms of computer speed, thus allowing for much better resolution of the subsurface (see Ledo 2005; Baba *et al.* 2006; Martí *et al.* 2009; Muller *et al.* 2009; Spratt *et al.* 2009; Garcia & Jones 2010; Ledo *et al.* 2011; Miensopust *et al.* 2011; Rosell *et al.* 2011, for examples of modern 2- and 3-D inver-

sion of MT data). Moreover, due to the shorter computation time of 2-D inversion, investigators can efficiently and effectively explore model space through varying options for inversion parameters and parametrizations, and examine various aspects of subsurface regions through hypothesis testing, for example, by using different *a priori* models or by removing features of an inversion model and examining whether they are re-introduced in subsequent inversion steps. Models of 3-D inversion are often taken and presented as 'like it or lump it', as computational cost prohibits calculation of

additional inversion steps. However, the validity of 2-D inversion needs to be tested for cases where the electric resistivity structure of the subsurface is potentially 3-D to some extent, since not taking into account the effects of 3-D structures can severely corrupt resulting models.

Different 2-D inversion approaches have been applied to 3-D subsurface cases before, but respective models have to be regarded with suspicion, as discussed in the comprehensive overview about 2-D interpretation approaches for 3-D subsurface cases given by Ledo (2005). For example, during their approach, using interpolation of Z_{yx}-only 2-D inversions to image 3-D structures of the Pannonian Basin (Hungary), Tournerie & Chouteau (2005) noted that responses from 3-D forward modelling of their interpolated model were significantly different for Z_{xy} periods related to deeper regions (>20 s). The authors related this discrepancy to unaccounted for anisotropic structures in the subsurface. However, Z_{xy} data, with the electric component orthogonal to the profile (i.e. TE in 2-D MT inversion[1]), are commonly assumed to be more affected by small-scale 3-D bodies due to charge build-up on the off-profile boundaries of these small-scale bodies (e.g. Jones 1983; Wannamaker *et al.* 1984; Berdichevsky *et al.* 1998; Ledo *et al.* 2002; Ledo 2005; Siripunvaraporn *et al.* 2005). Hence, 3-D inversion appears to be required for the Pannonian Basin region.

One particular 3-D subsurface case consists of lateral changes in electric conductivity along regional-scale interfaces with varying orientations of the interfaces at depth, for example, at crustal and mantle depths. Such a case might emerge, for instance, where crustal faulting, originating from present day tectonics, is situated above a mantle where structures are dominated by prior plate tectonic processes; for example, continental collision from an oblique direction. Cases of oblique geoelectric strike directions for different subsurface regions are a known problem in MT investigation, and have previously been reported by, among others, Marquis *et al.* (1995), Eaton *et al.* (2004), Wu *et al.* (2005), Miensopust *et al.* (2011) and Schmoldt & Jones (2013). Whereas recovery of upper (crustal) structures can usually be achieved in a straightforward manner by confining the modelled frequency range to crustal penetration depths, deriving deeper (mantle) structures is more challenging. Presently, no perfect solution is known to the problem of recovering mantle structures for cases of significantly oblique strike directions, save for full 3-D inversion with a large mesh.

Miensopust *et al.* (2011) inferred varying strike directions for their profile in northeastern Botswana, and used separate focussed inversions with different geoelectric strike directions to enhance their modelling. The authors used a strike direction of 55° clockwise from north (N55E) for a subset of their model, whereas a strike direction of N35E was used for the rest of the model. However, an extension of the approach by Miensopust *et al.* (2011) to a case with more oblique geoelectric strike directions is not straightforward. In such a case, decomposition of the impedance tensor in at least one of the regions will be significantly erroneous, and TE and TM mode estimates for the deeper regions will be related to incorrect depths (Jones 2006). A simple 'stitching' of inversion models from

different strike directions is therefore highly likely to yield a model in which structures of the deeper region are misrepresented.

In the PICASSO Phase 1 investigation (Schmoldt 2011; Schmoldt & Jones 2013), varying geological strike directions with both depth and along the profile are defined for the region of the Tajo Basin, Spain. Geoelectric strike direction in the Tajo Basin crust is approximately NW–SE, coinciding with the direction of the Iberian Range and Neogene faults, whereas at mantle depths a dominant NNE–SSW direction is observed (Schmoldt 2011). The defined change in strike direction is supported by results from seismic tomography studies (Bijwaard *et al.* 1998; Villaseñor *et al.* 2003, 2007), inferring a NW–SE directed interface at crustal depth and a NE–SW direction for deeper regions. Based on their orientation, a correlation with alpine orogenies that formed the approximately NW–SE stretching Pyrenees and the NE–SW stretching Betics during Late Mesozoic–Cenozoic times (e.g. Gibbons & Moreno 2002, and references therein) seems likely.

Computational cost of 3-D inversion is high, preventing detailed inversion of a region with the multi-scale size of the Tajo Basin. On the other hand, 2-D inversion requires the investigator to commit to one strike direction to be used for the inversion process, hence to invert data of at least one region with an erroneous strike direction assumption. This dichotomy motivated construction and examination of a synthetic modelling exercise that contrasts results of different inversion schemes and parameter settings for the case of oblique strike directions at crust and mantle depths. In particular, advances of novel algorithms that incorporate effects of anisotropic structures in the subsurface are utilized to recover structures at mantle depth.

2 THEORY

The MT method uses electromagnetic (EM) field variations to deduce the distribution of electric conductivity σ (or its inverse, electric resistivity ρ) within the Earth and through that the geological setting of the subsurface is derived. MT has been widely used for various geophysical applications since its development in the middle of the last century (Rikitake 1948; Tikhonov 1950; Cagniard 1953) and the interested reader is referred to the review paper series on MTNet (www.mtnet.info) for a comprehensive overview about the methods and its application, and to the new book by Chave & Jones (2012). Here, only aspects related to the novel inversion approach presented in this paper are recapped in brief.

It is common practice in MT to describe EM field relations in the frequency domain because the induction depth of an EM wave is proportional to its period. Relations between electric and magnetic fields at different periods, hence the electric conductivity, can therefore be related to different regions within the subsurface. In MT, relationships between all horizontal electric and magnetic fields are usually described using the 2×2 complex MT impedance tensor $\mathbf{Z}(T)$, which can be written in compact form as

$$\vec{E}(T) = \mathbf{Z}(T) \cdot \vec{H}(T) \tag{1}$$

$$\Leftrightarrow \begin{pmatrix} E_x(T) \\ E_y(T) \end{pmatrix} = \begin{pmatrix} Z_{xx}(T) & Z_{xy}(T) \\ Z_{yx}(T) & Z_{yy}(T) \end{pmatrix} \cdot \begin{pmatrix} H_x(T) \\ H_y(T) \end{pmatrix}, \tag{2}$$

where E_x, E_y, H_x, H_y denote respective horizontal components of electric and magnetic fields in the frequency domain related to the x- and y-directions in a given coordinate system, and T indicates the dependency on the period of the EM field.

---

[1] For a 3-D subsurface no alignment of Z_{xy} and Z_{yx} data with a 2-D electric resistivity interface can be made in the classical sense. Thus, TE and TM mode only denote 'transverse' in terms of 'transverse to the profile direction' and are not necessarily related to the orientation of a resistivity interface. With the profile along the y-axis, Z_{yx} is associated with the TM mode.

It is also common practice to describe the complex impedance tensor elements using the so-called apparent resistivity

$$\rho_{a_{ij}}(T) = \frac{1}{\mu\omega}\left|Z_{ij}(T)\right|^2 \qquad (3)$$

and impedance phase

$$\phi_{ij}(T) = \arctan\left(\frac{\Im(Z_{ij}(T))}{\Re(Z_{ij}(T))}\right), \qquad (4)$$

with $i, j \in [x, y]$.

For the case of a 1-D subsurface, that is, only vertical changes of electric conductivity, diagonal elements of **Z** are equal to zero and off-diagonal elements exhibit the same amplitude but different signs (e.g. Vozoff 1991), that is, $Z_{yx} = -Z_{xy}$. (Different signs of 1-D off-diagonal impedance tensor elements are due to the use of right- and left-hand coordinate systems for Z_{xy} and Z_{yx} elements, respectively.) For a 1-D subsurface the impedance tensor therefore reduces to

$$\mathbf{Z}_{1D} = \begin{pmatrix} 0 & Z_{xy}(T) \\ -Z_{xy}(T) & 0 \end{pmatrix}. \qquad (5)$$

When the subsurface comprises lateral conductivity interfaces in only one direction (with an arbitrary number of vertical conductivity changes), the original coordinate system used for the recording can be rotated by an angle Θ to fit the interface direction using a transformation tensor

$$\mathbf{R} = \begin{pmatrix} \cos(\Theta) & -\sin(\Theta) \\ \sin(\Theta) & \cos(\Theta) \end{pmatrix}. \qquad (6)$$

For the case of perfect adjustment of coordinate system and lateral conductivity interface direction, the impedance tensor reduces to

$$\mathbf{Z}_{2D} = \begin{pmatrix} 0 & Z_{xy}(T) \\ Z_{yx}(T) & 0 \end{pmatrix}, \qquad (7)$$

and eq. (1) to

$$E_x(T) = Z_{xy}(T)H_y(T), \qquad (8)$$

$$E_y(T) = Z_{yx}(T)H_x(T). \qquad (9)$$

In 2-D MT investigation, the x-axis is usually chosen parallel to the lateral conductivity interface and the y-axis is associated with the direction of the profile, which is optimally oriented orthogonal to the regional electric resistivity interfaces. Therefore, the remaining elements Z_{xy} and Z_{yx} comprise data of the electric component parallel and the magnetic component orthogonal to the resistivity interface and vice versa, respectively. Accordingly, Z_{xy} and Z_{yx} are commonly referred to as transverse electric (TE) and transverse magnetic (TM) mode response data, respectively.

Reducing the dimensionality of **Z** from 3-D to 2-D significantly reduces computational expense and time of inversion processes. Such a reduction of the dimensionality, however, is usually more challenging due to a complex subsurface structure where no straightforward alignment of the coordinate system with a single lateral interface is possible. One particular situation dealt with in this study is the case of two oblique strike directions at different depths.

3 NUMERICAL EXPERIMENT

3.1 The synthetic 3-D model

The synthetic 3-D model (Fig. 1) is created using the 3-D forward modelling program of the WinGLink software package (WinGLink 2005). The model features four blocks of different electric resistivity, with geoelectric strike directions of N45E ($+45°$) for the top 30 km and N45W ($-45°$) for the region below; in the following, the upper region will be referred to as 'crust' and the lower region as 'mantle'. The crust contains a conductive region (NE half) and a relatively resistive region (SW half) with electric resistivities of 50 Ωm and 200 Ωm, respectively. The relatively conductive region of the mantle (SE half) is assigned a resistivity of 500 Ωm, whereas the resistive mantle region has a resistivity of 1000 Ωm. The model is rotated clockwise by 45° to accommodate straight mesh lines at an angle $+45°$ and $-45°$, thereby avoiding edge effects of the rectangular mesh used for the finite difference (FD) modelling (e.g. Cerv & Pek 1990; Avdeev 2005; Börner 2010). MT responses are modelled for the period range 10^{-3}–10^5 s at 144 stations arranged in a grid on top of the synthetic model as well as for 13 additional sites aligned along an approximately N–S oriented profile (*cf.* Fig. 2).
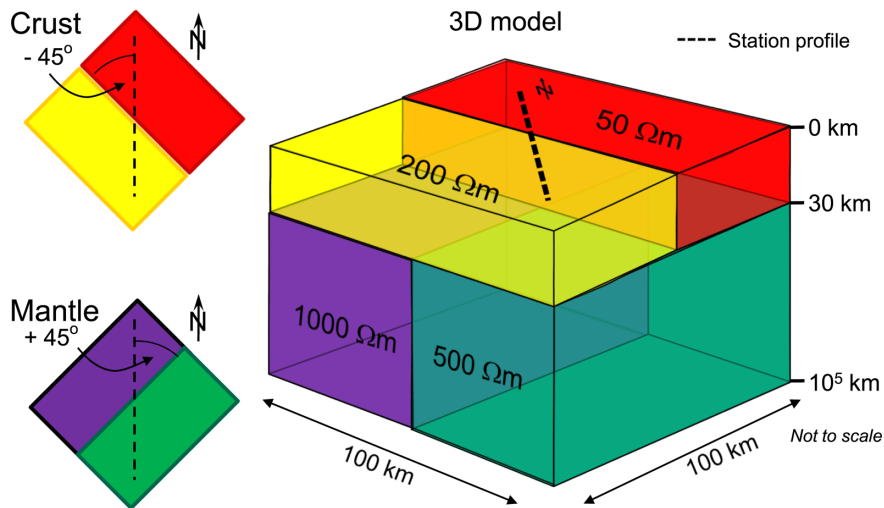
Figure 1. Subsurface model with orthogonal geoelectric strike directions at crust and mantle depths. Constructed to derive an optimized 1- or 2-D inversion approach that provides an optimal recovery of the resistivity distribution at mantle depth for such a case of oblique strike directions in crust and mantle. Please note, that the models comprise isotropic inhomogeneities not anisotropy. The approximate location of the N–S directed profile is indicated by the dashed line.
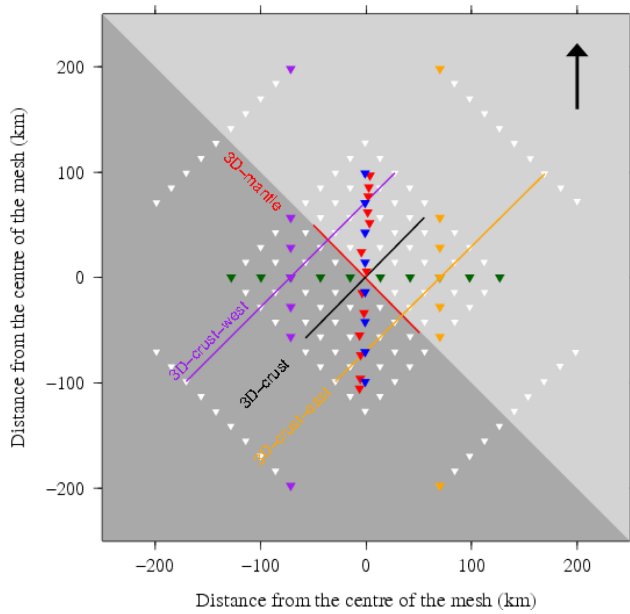
Figure 2. Location of magnetotelluric (MT) recording sites and profiles on top of the synthetic 3-D subsurface model (Fig. 1); north is located to the top of the figure. Displayed are 144 station arranged in a grid (inverted triangles), as well as 13 additional sites along an approximately N–S oriented profile. Background colours indicate the relatively conductive (light-grey) and resistive (dark-grey) regions of the crust; the location of the resistivity interface at mantle depth coincides with the 3-D-crust profile (*cf.* Fig. 1). The course of 2-D inversion profiles are indicated by the labels added to the plot; profiles are constructed orthogonal to the geoelectric strike direction of either crust or mantle and station locations are projected onto the profile. Profiles 3-D-crust and 3-D-mantle coincide with the conductivity interfaces at mantle and crust depth, respectively. Stations are associated with profiles of the same colour; for the profile labelled '3D-crust' three different sets of stations are used: red (3D-crust, using stations syn001–syn020), blue (3D-crust-NS), and green (3D-crust-EW). Every profile contains at least one station on top of each of the four electric conductivity regions (two at crustal depth, two at mantle depth), to assure that data of every profile are affected by the oblique strike directions.

3.2 Data preparation and analysis

Data obtained through forward modelling responses for stations on top of the 3-D subsurface are modified in order to meet requirements of the different inversion programs used in this investigation. For this purpose two different types of data sets are created, 'rotated' and 'decomposed', which are used for anisotropic and isotropic inversion processes, respectively.

Creation of the first data set simply involves rotating of data from all stations to N45W and N45E, that is, the respective strike directions of crust and mantle: Note that TE and TM modes are swapped for data sets with a difference of rotation by 90°. For these rotated data sets, diagonal elements of the impedance tensor are in general non-zero and are used for the novel anisotropic inversion approach.

The second data set (decomposed) is created using the program strike by McNeice & Jones (2001), based on the theory by Groom & Bailey (1989), commonly used in MT investigation to provide data sets suitable for isotropic 2-D inversion. The strike programme seeks to decompose the impedance tensor into contributions from regional 2-D conductivity structures and effects from near-surface galvanic distorting sources, thereby providing an impedance tensor that solely contains effects of the regional 2-D structure and is suitable for 2-D MT modelling. With the strike programme, two

data sets are generated that meet the strike directions at either crustal depth (N45E) or mantle depth (N45W). For these decomposed data sets, the diagonal elements of the impedance tensor (Z_{xx} and Z_{yy}) are considered insignificant and are not used during isotropic 2-D inversion.

Prior to inversion of forward responses from the synthetic 3-D model, the data are analysed to identify characteristics of the responses that provide understanding on the applicability of the different inversion approaches. First, the response data are visualized using maps of four different periods (periods are used as a proxy for depths), in which north is located towards the top left (Fig. 3); the figures are rotated counterclockwise by 45° (with respect to Fig. 2) to accommodate plotting of multiple maps side by side. Using Niblett–Bostick depth estimation (Niblett & Sayn-Wittgenstein 1960; Bostick 1977) yields that on the resistive side periods greater than 18 s (approx. 1.26 in log-scale) penetrate into the mantle, whereas on the conductive side penetration into the mantle is first achieved by periods half a decade longer at 72 s (approx. 1.86 in log-scale). In Fig. 3 '*XY* data' refers to the TE mode, and '*YX* data' refers to TM mode, for the data set adjusted to the crustal strike direction (N45W), whereas the '*XY* data' refers to the TM mode and '*YX* data' refers to TE mode for the data set adjusted to the mantle strike direction (N45E). The similarity of crustal TE and mantle TM data (and vice versa) is due to the 90° difference between the two strike directions, resulting in swapping of the two modes. Different colour scales are used to display values in maps of different modes and periods (rather than using uniform colour scale values) to highlight structures at the respective period. Note that, in order to enable plotting of all phase data in the first quadrant (0° – 90°), 180° is added to the respective *YX* phase data.

At shorter periods (0.01 s, top-left plots in Fig. 3), responses are dominated by characteristics of crustal structures. Values for the two modes are alike, and $\rho_a = \rho$; hence $\rho_a = 50\,\Omega m$ (approx. 1.7 in log-scale) in the northeastern half and $\rho_a = 200\,\Omega m$ (approx. 2.3 in log-scale) in the southwestern half.

At longer periods (100 s, top-right plots in Fig. 3) mantle structures start to add observable contributions to the response data. Values of ρ_a at 100 s are similar to values of ρ_a at 0.01 s (note the different colour scale), but ϕ differs significantly. In general, $\phi(100\,s) < \phi(0.01\,s) \approx 45°$ owing to the more resistive nature of mantle regions with respect to the crust. At 100 s periods, the skin depth for stations on the resistive side of the crustal fault is approx. 70 km, whereas on the conductive side it is approx. 35 km. Thus, by 100 s period all sites are sensitive to the electric properties of the mantle. Phase anomalies at 100 s exhibit a point symmetry with regards to the centre of the station array, that is, where crust and mantle interfaces intersect. Phase anomalies are a superposition of effects from crustal and mantle structures with the anomaly magnitude (i.e. the absolute difference of ϕ values from 45°) being controlled by the resistivity difference between the crust and mantle (highest in the northern quadrant: 50 to 1000 Ωm) and the induction depth (greater in the southwestern half).

Response data for periods around 1000 s (bottom left plots in Fig. 3) also exhibit point symmetry, with the strongest phase anomalies (lowest ϕ values) located in the northern quadrant. In the southwestern half, phase values are closer to 45°, and apparent resistivity values are closer to the true resistivities of the synthetic model mantle owing to the higher resistivity of local crustal structures and the resulting greater induction depth.

Responses for the longest periods of the data set (6×10^4 s, bottom-right plots in Fig. 3), are still affected by distortion caused by crustal structures. Phase data for both modes differ between the
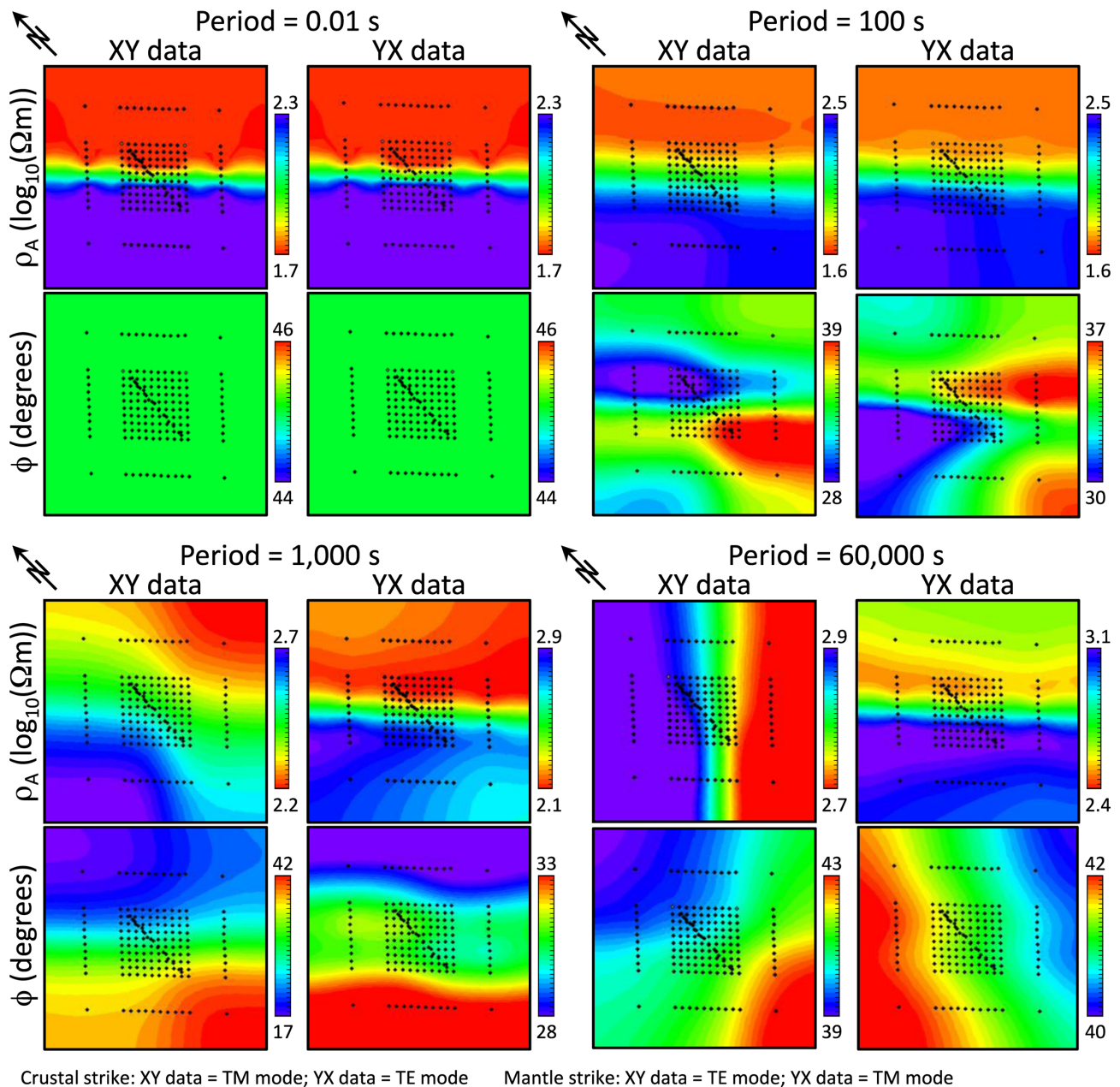
Figure 3. Maps of apparent resistivity (ρ_a) and impedance phase (ϕ) of the 3-D synthetic model (Fig. 1) at four periods representing different regimes; see text for details. Note that different colour scales are used to highlight structures of each plot. Plots are rotated anticlockwise by 45° with respect to Fig. 2 in order to accommodate plotting of multiple figures side-by-side; as a result north is located towards the top-left.

four quadrants (N, S, E, W), thus indicating effects from different induction depths and resistivity contrasts of the regions. The ρ_{xy} data are similar to mantle values of the synthetic model (1000 Ωm in the northwestern half, and 500 Ωm in the southeastern half), however, the ρ_{yx} values are significantly different. The *YX* data at long periods exhibit significant distortion effects, originating from the crustal structures and the orthogonal strike directions between the two depth regions. The ρ_{yx} data of the southern quadrant are higher than for the northern quadrant, resulting in an issue concerning, in particular, profiles using the stations of the approximately N–S oriented profile (syn001–syn020, denoted by red symbols in Fig. 2). The circumstance that the *YX* responses of the southern mantle region are significantly more resistive than the responses in the northern mantle region is reflected in TM mode data of the

crustal strike direction and TE data of the mantle strike direction (see also Fig. 4).

The pseudo-section (gridded resistivity–period values beneath the profile, in which period is used as a proxy for depth) for the N–S line (stations syn001–syn020 in Fig. 4) is displayed here as these stations form the most challenging combination by containing stations from each resistivity region of the synthetic 3-D model. Due to the characteristics of the 3-D model, two profiles are created with data arranged according to the geoelectric strike directions at crustal depth (N45W, left-hand side plot in Fig. 4) and mantle depth (N45E, right-hand side plot in Fig. 4); see Fig. 2 for the location of the profiles. Data from the crustal strike TE mode are similar to mantle strike TM mode data, and vice versa, because of the 90° difference between the two strike directions. Small variations in
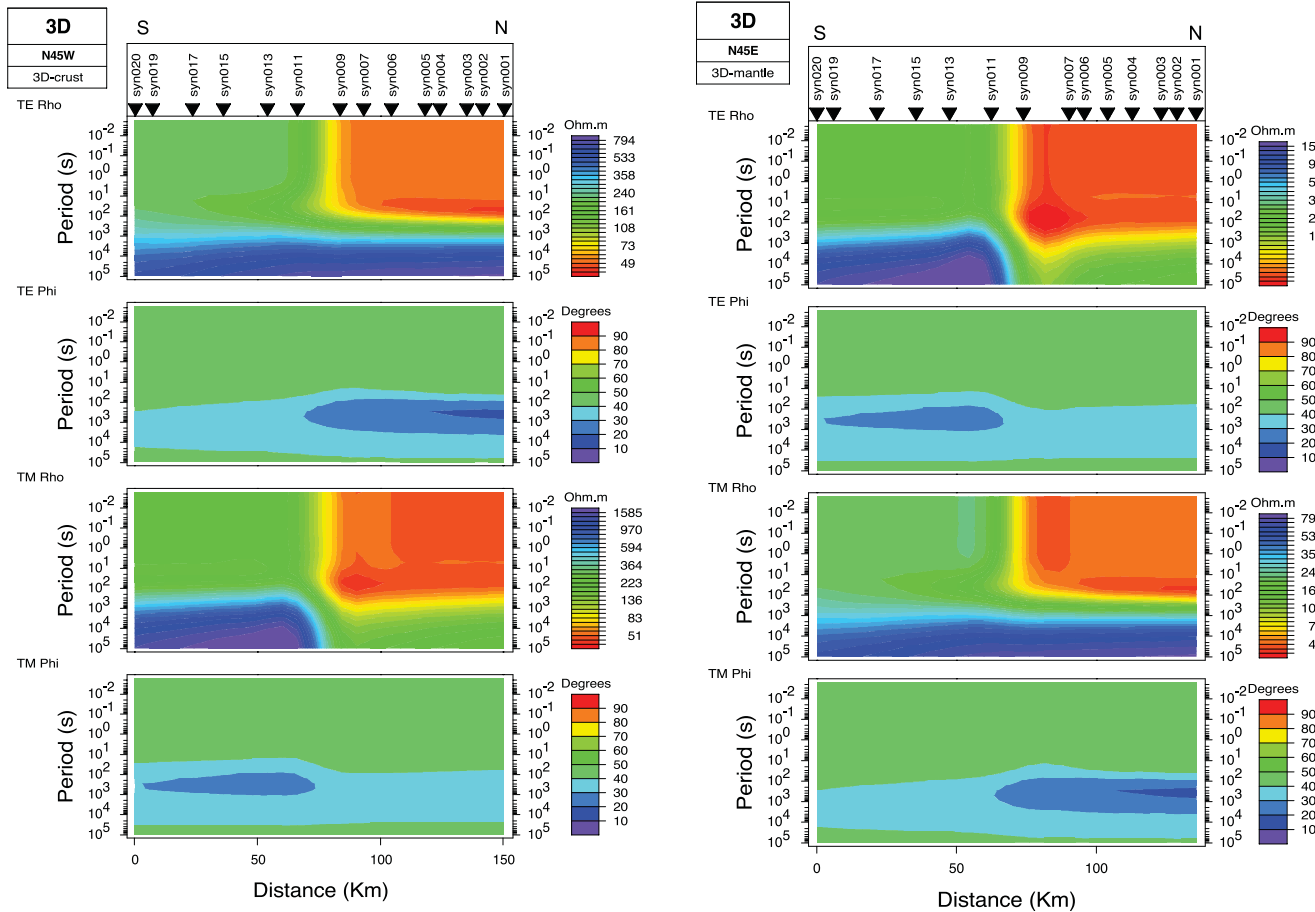
Figure 4. Pseudo-sections of the profiles 3-D-crust (left-hand side) and 3-D-mantle (right-hand side) with stations representing the MT recording sites of the approximately N–S oriented profile; see Fig. 2 for the location of stations and profiles. The northern end of the profile (NE for 3-D-crust profile, and NW for 3-D-mantle profile) is shown to the right.

the two pseudo-sections are due to the fact that the stations along the N–S oriented profile are not located equidistant along a line, and the resulting variation in projection of stations onto the profile. For both profiles and both modes, crustal probing periods ($T \leq 10^2$) exhibit a phase of approximately 45° and resistivities that are close to values of the synthetic 3-D model for regions beneath the respective site locations. Furthermore, the resistivity interface at crustal depth between stations syn009 and syn011 is clearly marked.

The values of the two modes differ significantly in the period range related to the mantle. In the following, the nomenclature of the modes is according to the mantle strike assignment (right-hand side plot in Fig. 4), that is, '*XY* data' refer to the TM mode and '*YX* data' refer to the TE mode; the important distinction that mode nomenclature is opposite for the crustal strike direction is omitted from here on. The sites are along a N–S profile and the strike of the mantle structure is NE–SW (Fig. 1), so the coordinate system for the data in the crustal strike direction of NW–SE is with *X* along NW–SE and *Y* along NE–SW. At mantle depths, the range of apparent resistivity for the TE mode (E parallel to mantle strike) exceeds the TM mode range: values for the TE mode range from 200 Ωm (northern end) to 1500 Ωm (southern end), whereas the TM mode values are mostly confined to a range 300–700 Ωm. It should be noted that the relative distribution of the TE mode apparent resistivities is opposite to the true model, which exhibits higher resistivity values in the northern mantle region than in the southern mantle region (*cf.* Fig. 1). Apparent resistivity values of the TM

mode are higher in the northern mantle region than in the southern region, thus it is more similar to the synthetic model.

A noteworthy issue of the TM mode data, however, is the apparent greater inductive depth of the southern mantle region (best observable in the phase data) even though the resistivity of the respective crustal region is higher than its northern counterpart. Accordingly, the interface between crust and mantle would be sensed at shorter periods in the south than in the north. The discrepancy must therefore originate from the oblique geoelectric strike direction of the synthetic model at crust and mantle depths, making it a challenging model for 1- and 2-D inversion and thus a good test for the novel inversion approaches.

4 INVERSION OF 3-D MODEL DATA

Recovery of subsurface structures using MT data currently most often consists of isotropic 2-D inversion of MT stations assigned along a linear profile during which the effects of near-surface and subsurface 3-D bodies are regarded as distortion and are removed where possible, for example, Garcia & Jones (2001), Brasse *et al.* (2002), Pous *et al.* (2004), Tournerie & Chouteau (2005) and Wannamaker *et al.* (2009). Thorough descriptions of distortion effects in MT data and procedures used to remove such effects are given, among others, in the review papers by Jiracek (1990), Ledo (2005) as well as in the publications by Jones (1983), Berdichevsky

et al. (1989), Vozoff (1986), Bahr (1988), Jones (1988), Groom & Bailey (1989), Jones *et al.* (1989), Pellerin & Hohmann (1990), Groom & Bahr (1992), Habashy *et al.* (1993), Jones & Groom (1993), Chave & Smith (1994), Spitzer (2006), Utada & Munekane (2000), Weaver *et al.* (2000), Garcia & Jones (2001), McNeice & Jones (2001), Caldwell *et al.* (2004), Simpson & Bahr (2005), Poe *et al.* (2010), and in the recent chapter by Jones (2012).

Here, responses for the 3-D subsurface model are inverted with a range of isotropic 2-D inversion approaches in order to evaluate the limitations of the method and to identify an optimal isotropic inversion scheme for the case of oblique geoelectric strike directions at crustal and mantle depth (Section 4.1).

Owing to the inadequacies of isotropic 2-D inversions for the case of oblique geoelectric strike directions, anisotropic inversion approaches are developed to obtain superior subsurface models. Mathematical considerations and applications of the anisotropic 2-D inversion approaches are illustrated in Section 4.2. The anisotropic 1-D inversion is discussed in Section A1 of the Appendix.

4.1 Isotropic 2-D inversion

4.1.1 Inversion approach

Oblique strike directions at crustal and mantle depths of the synthetic 3-D model (Fig. 1) pose severe problems for isotropic 2-D inversion of MT responses. In isotropic 2-D inversion, impedance tensor data are decomposed (not rotated!) with respect to the geoelectric strike direction of the subsurface, following Jones & Groom (1993) and McNeice & Jones (2001), and stations are projected onto a linear profile that is orthogonal to the strike direction. Due to the characteristics of the 3-D model examined in this study, every profile will be parallel to the strike direction of one depth region when it is oriented according to the strike direction of the other. For example, a profile intersecting the N45W oriented crustal interface at a right angle has a direction of N45E and is therefore parallel to the mantle strike direction. Thus, off-diagonal elements of the decomposed impedance tensor, that is, TE and TM mode, will always be erroneously assigned (swapped) for one of the depth regions. As a consequence, artefacts will be introduced during the inversion of the respective depth region. Recovery of the crustal region can be achieved using a data set and profile that fit the crustal geoelectric strike direction and limiting the period range to those periods sensing only crustal depths, which may be different for the two modes (see Jones 2006). However, inversion for mantle structures will suffer from misrepresentation of either crustal or mantle structures, since long-period responses that sense the mantle region are also affected by crustal structures.

In isotropic 2-D inversion, various approaches can be conceived in order to recover the mantle structures: common tools are 'fixing' of pre-defined crustal structures, 'tear zone' application, 'static shift' correction and the use of 'smoothing parameters'. Fixing of structures at crustal depth is generally reasonable, as thereby the inversion is focussed onto the mantle region. For the same reason, the application of two tear zones (separating inversion for crustal and mantle structures) appears to be worthwhile; however, its practicability will be tested here since resulting effects are not clearly predictable for such a complex subsurface model. An inevitable misrepresentation of structures at crustal depth related to short-period data and consequent distortion effects (e.g. Jiracek 1990; Garcia & Jones 2001) on data at longer periods suggests the application of static shift correction (e.g. Jones 1988; Pellerin & Hohmann 1990).

The correct choice of smoothing parameters is a general issue in MT investigation and is dependent on characteristics of the subsurface.

The optimal choice and weighting of parameters in inversions for the mantle structures will certainly be very much dependent on the initial choice of whether to represent the crust by a homogeneous layer or by 'locally true' resistivity values (i.e. values of the crust, but with an oblique crustal strike direction). The problem of approximating the crust by a homogeneous layer is evident: long-period data at all stations are affected by overlying structures and will be related to the wrong depth regions when short periods are different from the approximation; for example, in cases where the crustal conductivity structure varies laterally. Wrong depth relations are related to the erroneous induction depth for data of affected stations (*cf.* Fig. 4).

4.1.2 Inversion process

To explore an optimal combination of parameters, isotropic 2-D inversion is carried out using the WinGLink 2-D inversion software (WinGLink 2005), based on the algorithm by Rodi & Mackie (2001), as well as the updated anisotropic version [v. 6.11 (Baba *et al.* 2006)] with an isotropic setting ($\tau_{iso} = 999\,999$). Inversions are conducted using a range of smoothing parameter values, with and without fixing of the crustal range, tear zone application and static shift correction, in order to determine an optimal set of inversion parameters for subsurfaces similar to the synthetic 3-D model. Control on smoothness and regularization is facilitated through adjusting three parameters, namely α, β and τ. τ is the standard regularization trade-off (Tikhonov) parameter between misfit and roughness. The smaller the value of τ the more the fit is emphasized; the larger the value, the more the smoothness is emphasized. α is the horizontal to vertical weighting factor, and multiplies the horizontal derivatives by that value to invoke greater horizontal smoothing. β is a weighting function that increases the penalty on vertical roughness as the block thickness increases with depth, and also increases the penalty on the horizontal roughness with depth in a way that is consistent with the implicit increase in vertical roughness. These parameters are described in more detail, and their effects shown in Matsuno *et al.* (2010). The smoothing parameter range comprises three different sets of parameter values: (1) increased values ($\alpha = 3$, $\beta = 1$, $\tau = 6$); (2) minimum values ($\alpha = 1$, $\beta = 1$, $\tau = 1$), which are likely to introduce a rougher model with more defined interfaces; and (3) intermediate values ($\alpha = 1$, $\beta = 1$, $\tau = 6$) with low constraints on the horizontal and increased constraints on the global smoothness, thus promoting vertical interfaces.

4.1.3 Inversion results

Due to manuscript length restrictions, only results for the '3-D-mantle' profile using stations syn001–syn020 (*cf.* Fig. 2) are shown here. Full results are shown in Schmoldt (2011). Impedance tensors of stations used for the 3-D-mantle profile are decomposed with respect to a geoelectric strike direction of N45E, that is, the strike direction of the synthetic 3-D model at mantle depths.

A number of inversion models with different subsurface characteristics fit the response data with an rms misfit <3, for error floors of $\rho_a = 20$ per cent and $\phi = 10$ per cent. (Note: the synthetic data only have an intrinsic noise level of machine precision, set to 10^{-21}, to avoid division by zero problems. Errors were assigned according to the error floors given.) MT, at least in one dimension, is proven to have a unique solution for perfect data at all frequencies
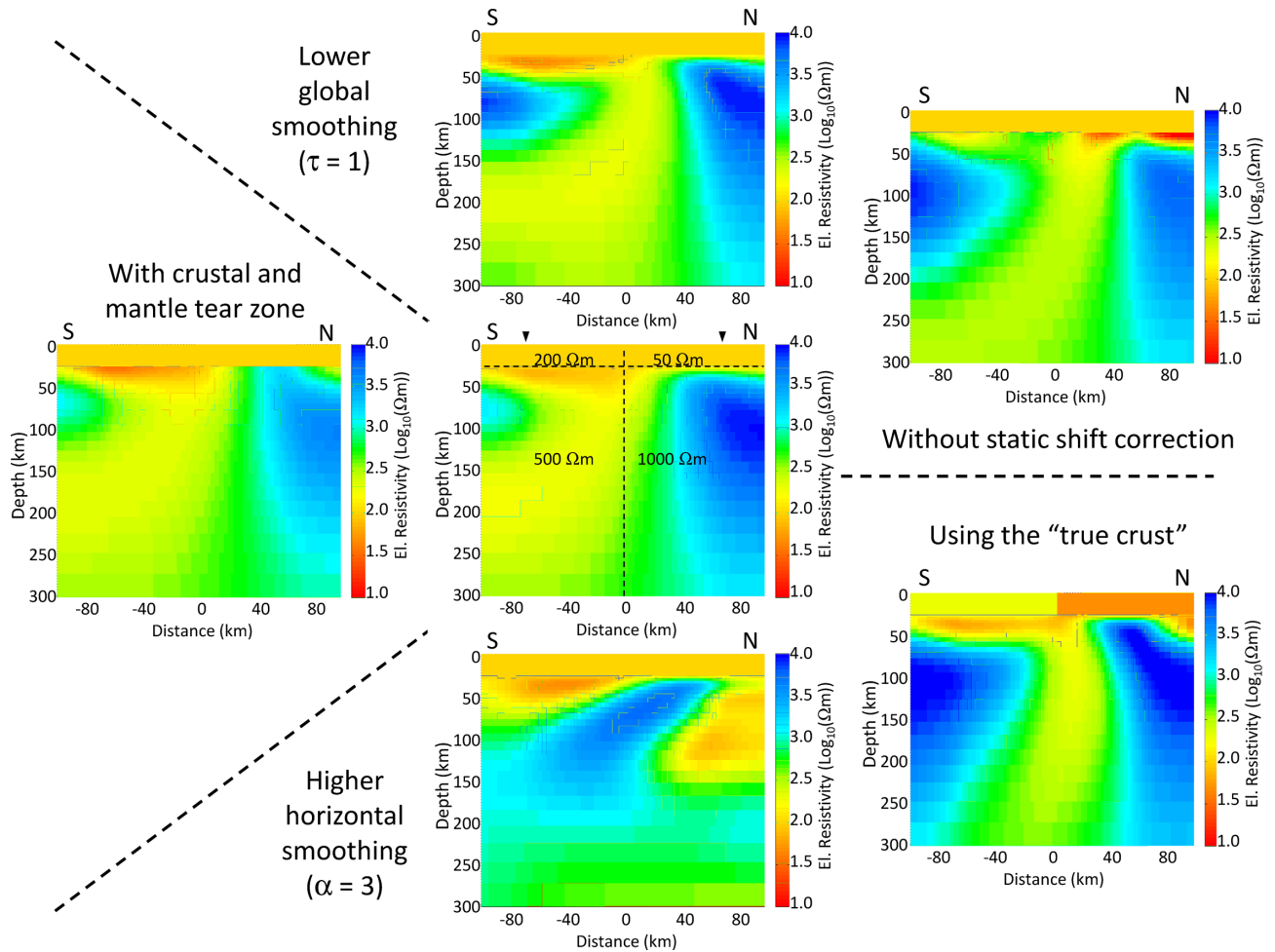
Figure 5. Selection of isotropic 2-D inversion models for a synthetic 3-D model with orthogonal strike direction at crust and mantle depth using the profile 3-D-mantle and the stations syn001–syn020 (*cf.* Figs 1 and 2). The true resistivity distribution beneath the profile is indicated on the central model together with the northern and southern ends of the profile, denoted by the inverted triangles. See text for details about the inversion settings.

(Tikhonov 1965; Bailey 1970; Parker 1983). However, data sparsity and inadequacy lead to the well-known non-uniqueness problem of MT inversion (e.g. Weidelt 1972; Parker 1980; Vozoff 1986; Constable *et al.* 1987). In here, the optimal inversion model is selected through comparison with the true subsurface model; see central plot in Fig. 5. A selection of additional inversion models is shown in Fig. 5 to illustrate effects of the different parameters that can be chosen to enhance the inversion model for the mantle region.

Through comparison of the models it becomes evident that a higher horizontal smoothing ($\alpha \geq 3$) increases the misfit and, moreover, yields models with a diagonal resistor, extending from 30 km at the northernmost stations of the profile down to a depth of approximately 200 km in the south. A low global smoothing ($\tau = 1$) decreases the misfit, but results in models with a more pronounced second resistor in the south of the profile at depths greater than 60 km. The lateral extent of the resistor depends on the choice of other inversion settings, such as static shift correction or the starting model resistivity of the crust.

In comparison with effects of different smoothing parameters, the influence of the remaining parameters is relatively small. Using a 'true crust', that is, the local crustal resistivity distribution of the synthetic model for the region beneath the stations (*cf.* bottom right plot in Fig. 5), increases the misfit significantly, and introduces

an additional resistive body in the left-hand side of the model. Increased misfit and the appearance of additional resistor are most likely a result of the incorrectly modelled crustal strike direction; during the inversion, a N45W strike direction is assumed for the crust (like for the rest of the model), whereas the synthetic 3-D model contains a N45E strike direction at crustal depth instead. Omitting a static shift correction causes, in general, a higher rms misfit for the case of a homogeneous uniform crust as well as for the case of the true crust. It is further confirmed that keeping crustal structures fixed is beneficial, as this focuses the inversion onto the deeper regions. On the other hand, using two tear zones to enforce effectively separate inversions for the crust and mantle parts of the model does not have a significant effect on the resulting model; this is presumably due to the fixing of the crust, which already enforces separate inversions.

It has long been suggested that TM mode data are less effected by 3-D anomalies (e.g. Ting & Hohmann 1981; Jones 1983; Wannamaker *et al.* 1984; Tournerie & Chouteau 2005), and that isotropic 2-D inversion of data from only the TM mode ('TM-only inversion') may therefore yield superior results. This hypothesis is tested here with the synthetic 3-D model using data sets decomposed according to the crustal strike direction (N45W, profile: 3-D-crust) as well as the mantle strike direction (N45E, profile: 3-D-mantle) for the
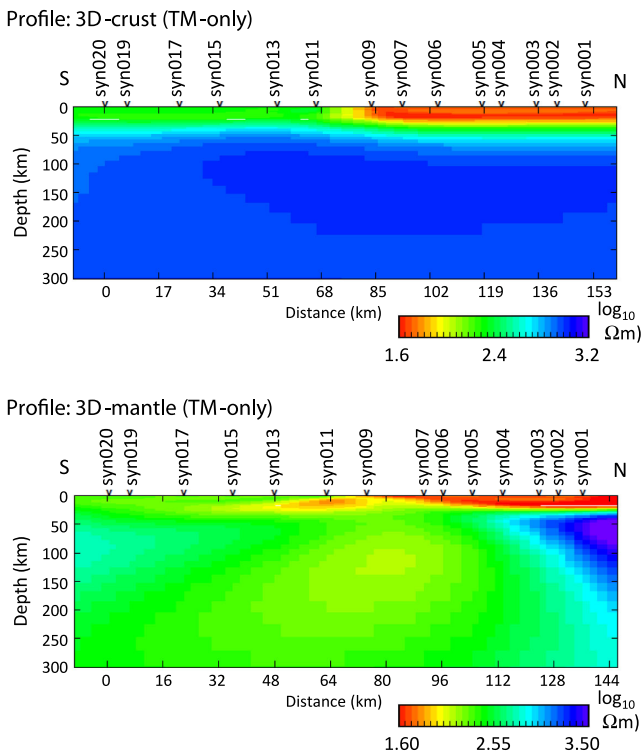
Figure 6. Result of isotropic 2-D inversion for the 3-D-crust (top panel) and mantle (bottom panel) profiles (*cf.* Fig. 2) using only data from the TM mode ('TM-only') of stations syn001–syn020. Data are decomposed according to the direction of the respective profile, that is, N45W for the 3-D-crust profile and N45E for the 3-D-mantle profile.

whole period range (10^{-3}–10^5 s) with the same smoothing parameters determined for the isotropic 2-D inversion with both modes. Results of the TM-only inversions indicate that this approach is not appropriate for the subsurface model used in this study, since respective models (Fig. 6) differ significantly from the electric resistivity distribution of the true model.

In conclusion, it has been found that approximating the crust by a 30-km layer and applying static shift correction during isotropic 2-D inversion yields models that are closest to the synthetic 3-D model (*cf.* central model in Fig. 5). However, even the model with the relatively best agreement with the true subsurface distribution suffers from a lateral shift of the resistivity interface towards the north (i.e. to the right in Fig. 5) and the introduction of a resistive body in the south of the model. Introduction of such artefacts needs to be kept in mind when interpreting results of isotropic 2-D inversions for similar subsurface cases. Using only data from the TM mode for the inversion did not result in a better agreement of inversion models with the synthetic 3-D model, hence we conclude that the TM-only inversion approach is not appropriate for the case of electric resistivity distribution with oblique strike directions.

Furthermore, the decision about the best subsurface model, hence the optimal combination of inversion parameters, is achieved through comparison with the true model. Selecting the best model for a case in which the subsurface is not *a priori* known will be more challenging and the doubt of ambiguity regarding the chosen model will remain, due to the non-uniqueness of MT inversion.

4.2 Anisotropic 2-D inversion

4.2.1 Inversion approach

Since the anisotropic 1-D inversion approach could be successfully applied to recover the synthetic 3-D model by imaging 2-D structures with a 1-D anisotropic region (*cf.* Section A1 in the Appendix), the principles are extended to 2-D inversions which do not suffer from the limitations of 1-D inversion, that is, facilitating more complex structures in the subsurface. In general, the coordinate system related to the 2-D regional structure and the coordinate system related to the anisotropy direction are not required to be identical. Therefore, anisotropic 2-D models have the potential to image effects of oblique strike directions in different subsurface regions by incorporating variable orientations of regional and anisotropy coordinate systems for the respective regions; this concept will be illustrated in the next paragraph.

Two contrary approaches can be conceived for anisotropic 2-D inversion of the 3-D model with oblique geoelectric strike directions in crust and mantle (Fig. 7): (1) isotropic 2-D representation of the crust and anisotropic imaging of the mantle, or, the opposite case, (2) anisotropic imaging of the crust and 2-D isotropic representation of the mantle (*cf.* Fig. 7). Imaging of the respective isotropic region is then according to eq. (7), whereas the anisotropic 2-D impedance tensor images the other region with the oblique strike direction

$$\mathbf{R}^T \cdot \mathbf{Z}_{2D} \cdot \mathbf{R} = \mathbf{Z}_{1D}^{ani}, \qquad (10)$$

with rotation matrix $\mathbf{R}$ defined in eq. (6), and $\mathbf{Z}_{1D}^{ani}$ defined in eq. (A1) in the Appendix. The two approaches differ in terms of the required rotation of the data sets as well as in terms of period range assigned to the isotropic and anisotropic part of the model. The latter determines whether the crust is assumed isotropic and the mantle anisotropic (approach 1, Fig. 7) or vice versa (approach 2, Fig. 7). The data set has to be rotated to fit the requirements of the
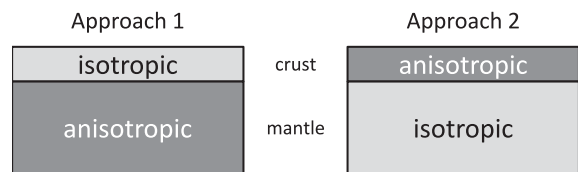

Figure 7. Approaches for anisotropic 2-D inversion of the 3-D subsurface model; see text for details.
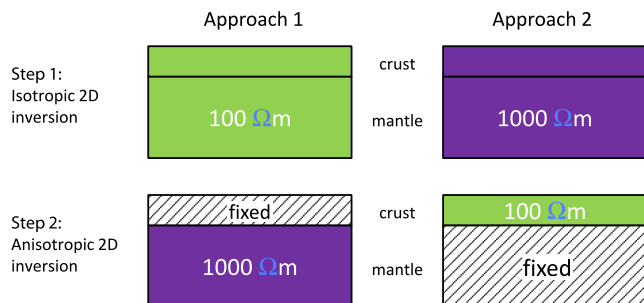

Figure 8. Starting models used for anisotropic 2-D inversion; see text for details about the two inversion approaches.

isotropic model part; that is, for the 3-D model used here, to N45W for the first approach and to N45E for the second.

4.2.2 Inversion process

In this study, the algorithm MT2Dinv-anis (Baba *et al.* 2006), an augmented, anisotropic version of the 2-D isotropic algorithm by Rodi & Mackie (2001), is used for the inversion. The algorithm requires that the anisotropy coordinate system is the same as the co-ordinate system chosen for the 2-D inversion, that is, the anisotropic conductivities σ_{xx}, σ_{yy}, σ_{zz} (e.g. Heise & Pous 2001; Pek & Santos 2006; Poe *et al.* 2010) denote conductivities parallel to the axes of the 2-D coordinate system. This limitation does not impair the anisotropic inversion approach for the 3-D subsurface model used in this study, as the two different geoelectric strike directions in the crust and mantle are orthogonal to each other. Alignment of the two strike directions with one of the two horizontal axes of the model can be achieved through either a clockwise or an anticlockwise rotation of the data set by 45°, that is, to N45E or N45W. The sense of the data set rotation, hence alignment of *x*- or *y*-axis with either strike direction at crust or mantle depths, depends on the inversion approach.

The current version of the MT2Dinv-anis algorithm does not permit the assignment of 'anisotropy zones' to the subsurface model, that is, it is not possible to separate the model into isotropic and anisotropic parts. Instead, the program only permits a global definition of an isotropy parameter τ_{iso}, which controls the anisotropy constraint in the objective function (Baba *et al.* 2006). Therefore, anisotropic 2-D inversion has to be carried in two sequences: first isotropic 2-D inversion of shorter periods, followed by anisotropic 2-D inversion for the mantle range (approach 1, Fig. 8) or isotropic inversion of long-period data followed by inversion of crustal-range periods (approach 2, Fig. 8). In approach 1 (Fig. 8), the first inversion sequence is carried out with a 100 Ωm half-space starting model, whereas the second sequence uses a starting model with crustal values derived in the first sequence and mantle values set to 1000 Ωm. In approach 2 (Fig. 8), the first inversion sequence is carried out with a 1000 Ωm half-space starting model and the second sequence uses a starting model with mantle values derived in the first sequence and crustal values set to 100 Ωm.

In this work, the focus is on advances of anisotropic 2-D inversion in contrast to an isotropic approach. The effect of different inversion parameters (smoothing, static shift correction, tear zone application) is a highly involved issue by itself and a detailed discussion would go beyond the scope of this paper. In the following the optimal smoothing parameter values ($\alpha = 1$, $\beta = 1$, $\tau = 6$), identified during isotropic 2-D inversion, are used (see Schmoldt (2011) for details regarding derivation of the smoothing parameters). As the aim of this anisotropic inversion approach is to use anisotropic 'distortion' to recover the 3-D subsurface structures, no static shift corrections or tear zones are applied, and the crust is neither fixed as a homogeneous layer nor with its 'true values'. Instead, crustal structures are determined in the course of the inversion process.

4.2.3 Inversion results

As for the cases of isotropic 2-D and anisotropic 1-D inversion (*cf.* Section A1 in the Appendix), evaluation of anisotropic 2-D inversion results in this paper is focussed on the stations syn001–syn020. Results for other profiles are added at the end of this section. In general, anisotropic 2-D inversion is reason-

ably fast; for most profiles, inversions of one sequence is carried out in under 4 hr using one processor of a Dell Intel Xeon CPU X5680 dual core machine with 3.33 GHz for a mesh with 108×146 cells and 1600 data points (product of number of stations, number of period estimates and impedance tensor elements).

The MT2Dinv-anis inversion algorithm (Baba *et al.* 2006) yields electrical resistivity models for the direction parallel and orthogonal to the profile, that is, ρ_{xx} and ρ_{yy}. Thus, no rearrangement of data vectors for the different cells of the model, as in the case of anisotropic 1-D inversion, is required. The ρ_{xx} model can be used to recover the resistivity distribution of the region that is not in agreement with the assumption of isotropic strike direction; that is, the mantle in approach 1 and the crust in approach 2 (*cf.* Fig. 7).

The second approach currently suffers from a systematic problem. Long-period data, sensing the mantle region, are affected by the resistivity distribution of regions above. Hence, results obtained in step one are biased and, even though crustal structures can be recovered to some degree using anisotropic inversion during step 2 (i.e. values of crustal resistivity of the inversion model are similar to the synthetic model), mantle structures remain erroneous. Subsequent isotropic inversion of the mantle (in a third inversion sequence) destroys the anisotropic crustal structures due to the inherent isotropy constraints. An anisotropic inversion in the second sequence, on the other hand, contradicts the anisotropic inversion approach by introducing anisotropic features to the mantle. For successful application of the second anisotropic inversion approach 'anisotropy zone' assignment is required, but this is not implemented. As a result, realization of approach 2 has to be postponed for the time being. This is unfortunate, since approach 2 is likely to yield excellent inversion results for the mantle given its isotropic (instead of anisotropic) inversion of mantle range using the true mantle strike direction. It is therefore strongly recommended that performance of the second approach is thoroughly investigated, once anisotropy-zones are implemented in the inversion code.

Approach 1 does not suffer from the lack of anisotropy-zones, because the isotropic inversion of shorter periods is conducted prior to the anisotropic inversion of long-period data. Fixing the crustal structures at their isotropic values does not impede anisotropic inversion in the secondary sequence, and approach 1 yields ρ_{xx} inversion models that exhibit resistivity distributions similar to the true model (*cf.* Fig. 9). Crustal structures are recovered reasonably well for both anisotropy directions (ρ_{xx} and ρ_{yy}) and in the ρ_{xx} model the resistivity interface at mantle depths is considerably well resolved. The ρ_{xx} model exhibits a distinct lateral change from intermediate resistivity values in the south of the profile to high resistivity values in the north, whereas the ρ_{yy} model contains a less distinct lateral change. The change of electric resistivity is facilitated through a changing degree of anisotropy magnitude (ρ_{AA} plot in Fig. 9).

Exceedingly high values of the northern mantle region as well as smooth variation in anisotropy magnitude, hence the less distinct lateral interface in the ρ_{xx} model, are due to the applied smoothness constraints of the inversion process. The agreement of ρ_{xx} inversion models with the synthetic 3-D model can be enhanced by choosing a lower smoothing parameter τ and a resistivity gradient regularization (instead of a Laplacian regularization) for the objective function of the inversion process (*cf.* Fig. 10). The misfit for the inversion models, obtained through inversion with different smoothing parameters, is generally low (rms misfit ≤2 with a 5 per cent error floor for impedance phase data and a 10 per cent error floor for apparent resistivity data) and evenly distributed between the different periods and stations.
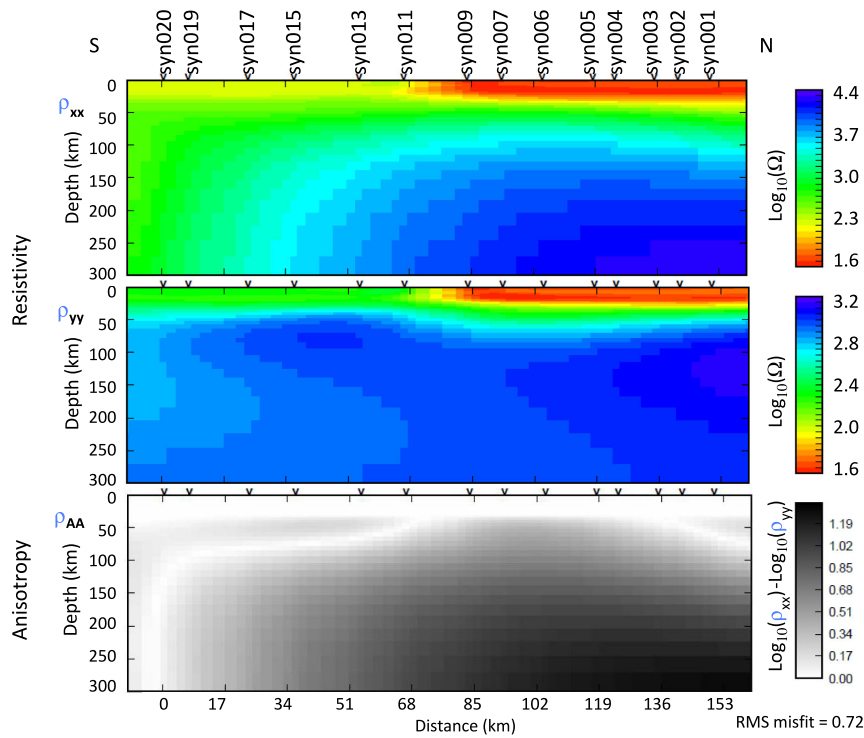
Figure 9. Anisotropic 2-D inversion results for the 3-D-crust profile over the synthetic 3-D body (Fig. 1), using data from the stations syn001–syn020 [*cf.* Fig. 2. A horizontal electric resistivity interfaces is located at a depth of 30 km and vertical interfaces are located between stations syn009 and syn011 (at crustal as well as at mantle depth)]. ρ_{xx} and ρ_{yy} denote subsurface models of electric resistivity orthogonal and parallel to the profile, respectively; the ρ_{AA} model displays the anisotropy magnitude.
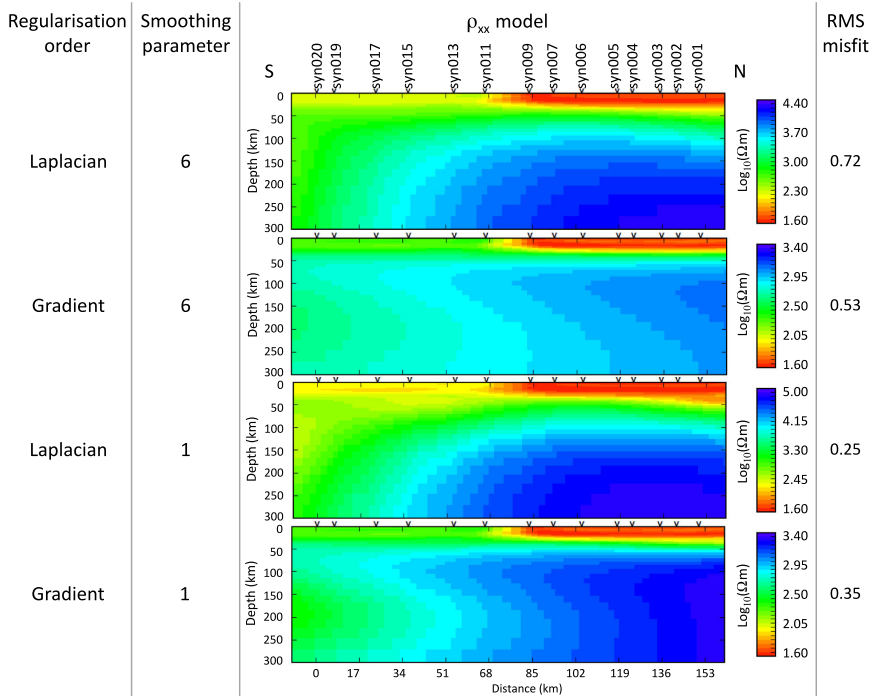

Figure 10. Comparison of ρ_{xx} inversion models for the profile 3-D-crust and stations syn001–syn020 using different smoothing parameters (note the different colour scales used for the models); see Fig. 2 for location of profile and stations.

For models from the 3-D-crust profile with stations syn001–syn020 generally a good agreement with the true subsurface is achieved. Adequate results are also accomplished for other profiles and data sets from different stations, providing a reasonable recovery

of the 3-D model (*cf.* Fig. 11). However, the selection of inversion parameters used is tailored to the characteristics of the 3-D model and its very localized changes of electric resistivity (e.g. from 50 Ωm to 1000 Ωm in the northern region of the model). Thus, for the case
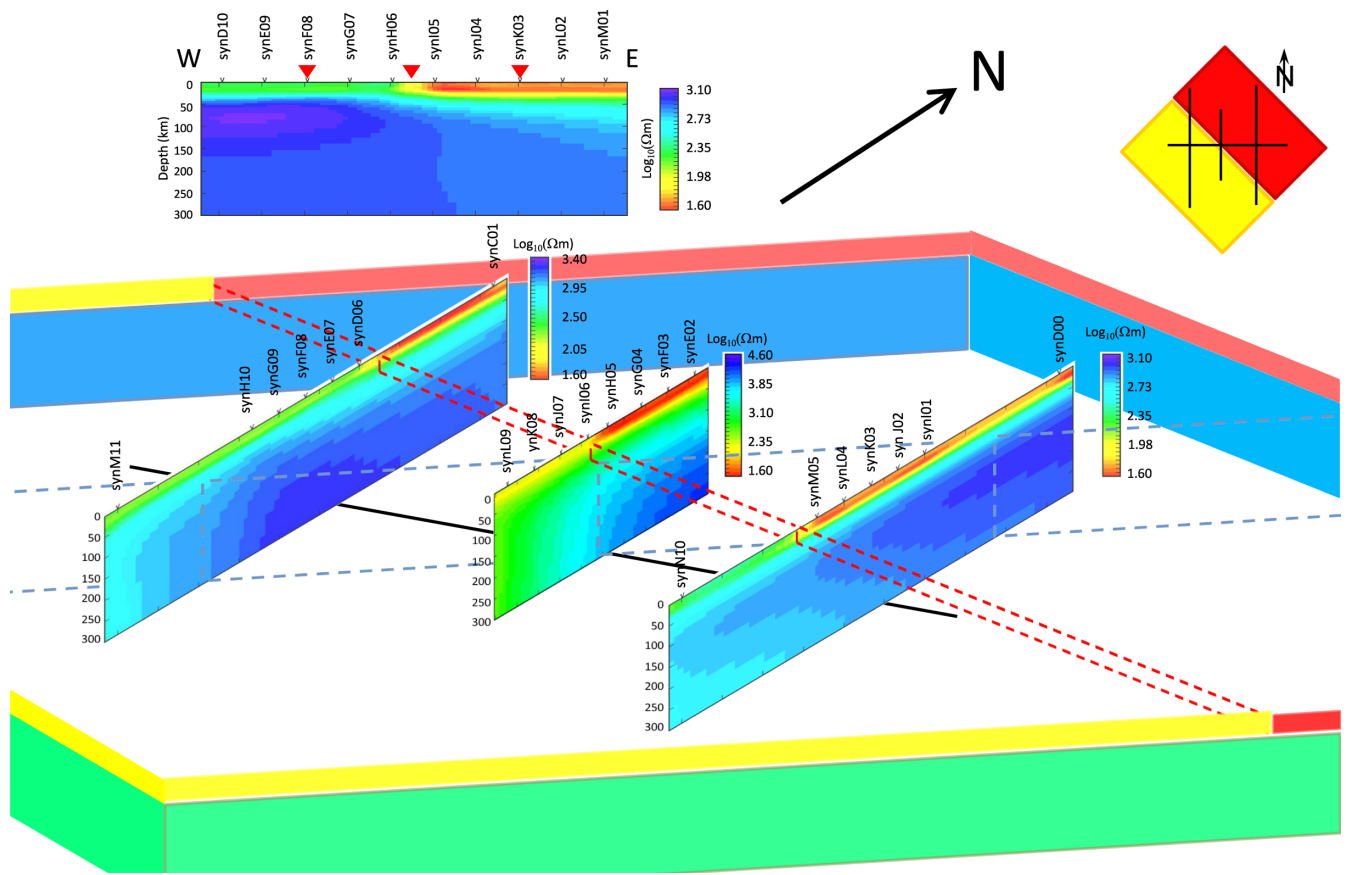
Figure 11. Results of anisotropic 2-D inversion of the synthetic 3-D model for a selection of profiles, from left to right: 3-D-crust-west with stations synM11–synC01, 3-D-crust-NS with stations synE02–synL09, and 3-D-crust-east with stations synN10–synD00, as well as 3-D-crust-EW profile with stations synD10–synM01 (upper most plot); see Fig. 2 for location of stations and profiles. Results are plotted in respect to the station locations; see black lines in the inset on the top-right of the figure. The solid black line in the main plot indicates the projected location of the 3-D-crust-EW profile result (model shown on the top of this figure), and red inverted triangles on the 3-D-crust-EW profile denote location of intersection by the other profiles. Dashed lines indicate resistivity interfaces of the synthetic 3-D model at crust (red) and mantle (blue) depth (*cf.* Fig. 1). For orientation, side panels are shown, which indicate regions of the synthetic 3-D model by colour, following the colouring of the synthetic model.

of real subsurface, with unknown distribution of electric resistivity, using a higher degree of smoothing may prove more appropriate.

In order to test robustness of the anisotropic 2-D inversion approach, inversion of the 3-D-crust profile is repeated for data with low, medium and high amount of added noise to the synthetic responses. For that purpose 1 per cent, 3 per cent and 10 per cent random noise is added to the data set, and inversion is carried out according to the second approach, with resistivity gradient regularization and high smoothing ($\tau = 6$). Inversion results for the three noise levels indicate that synthetic model structures can be resolved for low and medium amount of noise, whereas for higher noise levels the vertical resistivity interface at mantle is not well reproduced (*cf.* Fig. 12). For subsurface cases that are more complex than the synthetic model used in this study responses will be affected by noise as well as by additional geological features (e.g. small-scale bodies). Therefore, a smaller amount of noise may already result in a significant corruption of the data.

Anisotropic 2-D inversion is capable of recovering the electric resistivity distribution for a profile over a 3-D subsurface to a certain degree. That is, lateral changes of resistivity in the model are reproduced at crustal and mantle depths. However, sharpness and apparent lateral location of the interface at mantle depths are subject to the choice of smoothing parameters. Moreover, values of the resistive mantle region are less well constrained, and may

significantly exceed values of the synthetic model without adequate inversion constraints. For the 3-D model and parameter range used in this study, a combination of low smoothing parameter ($\tau = 1$) and resistivity gradient regularization yields an optimal model.

5 SUMMARY AND CONCLUSIONS

In order to investigate the performance of MT inversion programs for complex subsurface cases, a 3-D model with two orthogonal strike directions was created and results of different approaches were examined. For isotropic 2-D inversion, a set of inversion parameters was identified that yields a subsurface model closest to the original model (for this inversion approach). Whereas crustal structures were reconstructed reasonable well, the electric resistivity distribution of the mantle was not well recovered. Even the optimal isotropic 2-D model contains significant inversion artefacts, in particular a resistive body at mantle depths. Using only TM mode data for the isotropic 2-D inversion process did not result in a more adequate reproduction of mantle structures. Results of isotropic 2-D inversion for subsurface cases similar to the 3-D model used in this study are therefore to be used with caution.

Anisotropic 1-D inversion yielded models (Section A1 in the Appendix) that are close to the 3-D subsurface model, thereby
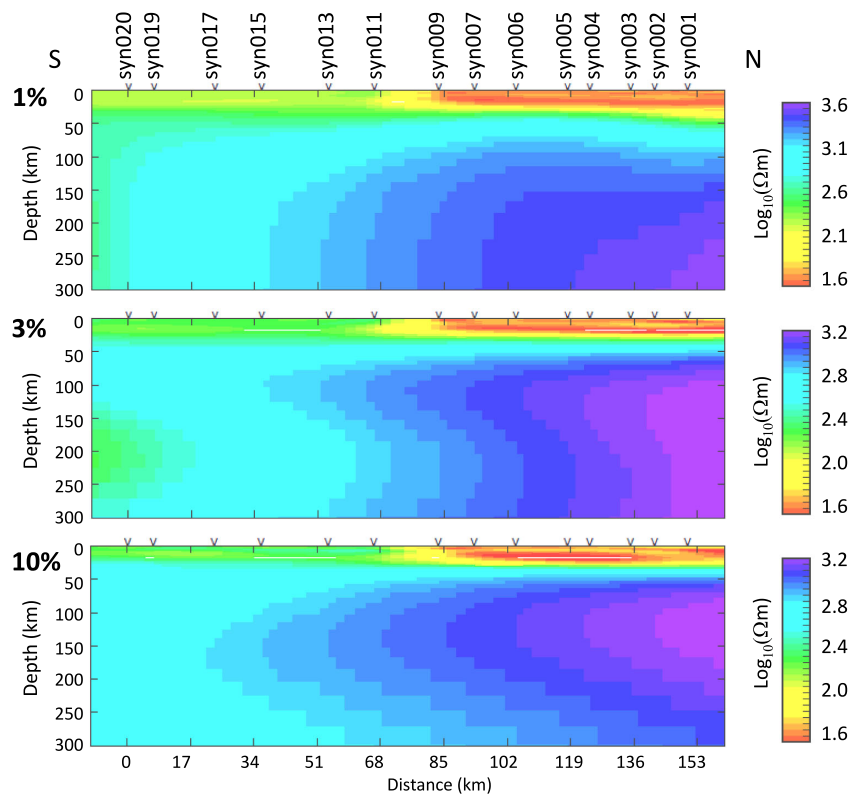
Figure 12. Results of anisotropic 2-D inversion for the 3-D-crust profile over the synthetic 3-D body (Fig. 1), using data from the stations syn001–syn020 (see Fig. 2 for profile and station locations), with 1 per cent, 3 per cent and 10 per cent random noise added to the data.

indicating the potential of anisotropic inversion for the case of complex subsurface structures. In the anisotropic 1-D inversion approach the crust was approximated by a quasi-isotropic 1-D layer and the mantle was imaged by an anisotropic 1-D structure. Crustal structures of the synthetic 3-D model were, in general, adequately reproduced by the anisotropic 1-D inversion; the vertical electric resistivity interface at crustal depths were imaged by a step-like change of resistivity between stations at the respective location. Mantle structures were recovered reasonably well using resistivity values for the anisotropy direction parallel to the mantle strike direction. The difference between the resulting inversion model and the synthetic model is, for most regions, below 10 Ωm. In particular, the northern part of the mantle is very well reproduced with differences of generally less than 5 Ωm. This finding demonstrates the practicality of anisotropic inversions in resolving certain types of 3-D subsurface models. However, due to the inherent limitations of 1-D inversion (e.g. less likely to adequately recover a model containing more complex structures), its results may not be used as a final model, but rather to aid subsequent 2-D anisotropic inversion, or to construct a 3-D initial model.

In the anisotropic 2-D inversion approach, anisotropic structures were introduced to certain regions of the model in order to account for effects of oblique geoelectric strike directions in different depth regions; that is, crust and mantle in our case. Those effects originate from the inevitable erroneous assignment of TE and TM mode in either crustal or mantle region during the 2-D inversion. The model used in this study features two orthogonal strike directions at different depth regions, and the coordinate systems used for the inversion were, in each case, aligned with one of the strike directions. Thereby, isotropic 2-D inversion of the region with the respective strike direction was facilitated. The electric resistivity

distribution of the other region can be recovered by models with an anisotropy direction parallel to the strike direction at the respective depth.

Due to limitations of anisotropic inversion algorithms, it is currently required that the isotropic region be located above the anisotropic region. The alternative approach, containing anisotropic inversion of the upper area and isotropic inversion of the lower area, has the potential to yield excellent inversion results for the mantle, hence thereby mantle structures are inverted for using isotropic inversion and the strike direction of the mantle. It is strongly recommended that investigation of the alternative approach is accomplished once respective suggestions have been implemented in the inversion algorithms. The approach described in this publication involves isotropic 2-D inversion for crustal structures and subsequent anisotropic inversion for mantle structures; therein initially obtained crustal structures are kept fixed. This approach yielded models of electric resistivity distributions that recover the 3-D model reasonable well.

Details about the location of the electric conductivity interface and values at mantle depths are subject to the choice of smoothing parameters used in the inversion, but generally inversion models provided useful information about the subsurface structures. It can therefore be concluded that anisotropic 2-D inversion is an adequate approach for investigations of subsurface regions with oblique geoelectric strike directions that do not require computational expensive and time-consuming inversion in the order of 3-D inversion. The anisotropic 2-D inversion algorithm used in this study, however, currently requires coincident directions of structural strike and anisotropy. Thus, the algorithm facilitates only a difference of 90° between the strike directions of crust and mantle. Hence, subsurface models obtained with the anisotropic 2-D inversion approach

for cases with oblique strike directions that are significantly different from the orthogonal case must currently be associated with a higher degree of uncertainty.

Further development of the anisotropic inversion approaches are strongly linked to enhancements of the inversion algorithms. Particularly useful enhancements of 2-D algorithms that would improve applicability of this novel inversion approach are:

(i) Incorporation of anisotropy-axes directions that are independent of the inversion mesh orientation. The 1-D inversion algorithm ai1d by Pek & Santos (2006) permits flexible anisotropy-axes directions, and the principle has been adopted for a 2-D algorithm with some success Pek *et al.* (2011). However, the 2-D algorithm is not yet optimized or adapted for parallel processing; thus, computation time of this algorithm is intractably long, limiting the realization to a very small number of impedance estimates and making its application to large data sets unfeasible.

(ii) Incorporation of 'anisotropy zones' in the inversion algorithm; that is, constraining anisotropy to a different degree for certain parts of the inversion model, similar to 'tear zones', which are already incorporated in current algorithms, for example, by Rodi & Mackie (2001).

Their implementation will enable future studies to investigate applicability of this novel approach to more complex subsurface cases. In addition, it is suggested to employ the approach in a wide range of synthetic and real model studies in order to further asses its performance.

ACKNOWLEDGEMENTS

REFERENCES

Avdeev, D.B., 2005. Three-dimensional electromagnetic modelling and inversion from theory to application, *Surv. Geophys.,* **26,** 767–799.

Baba, K., Chave, A.D., Evans, R.L., Hirth, G. & Mackie, R.L., 2006. Mantle dynamics beneath the East Pacific Rise at 17 degrees S: insights from the Mantle ELectromagnetic and Tomography (MELT) experiment, *J. geophys. Res., 111,* B02101, doi:10.1029/2004JB003598.

Bahr, K., 1988. Interpretation of the magnetotelluric impedance tensor: regional induction and local telluric distortion, *J. Geophys.,* **62,** 119–127.

Bailey, R., 1970. Inversion of the geomagnetic induction problem, *Proc. R. Soc. Lond. A. Math. Phys. Sci.,* **315**(1521), 185–194.

Becken, M., Ritter, O. & Burkhardt, H., 2008. Mode separation of magnetotelluric responses in three-dimensional environments, *Geophys. J. Int.,* **172**(1), 67–86.

Berdichevsky, M.N., 1999. Marginal notes on magnetotellurics, *Surv. Geophys.,* **20**(3), 341–375.

Berdichevsky, M., Vanyan, L. & Dmitriev, V., 1989. Methods used in the U.S.S.R. to reduce near-surface inhomogeneity effects on deep magnetotelluric soundings, *Phys. Earth planet. Inter.,* **53,** 194–206.

Berdichevsky, M., Dmitriev, V. & Pozdnjakova, E., 1998. On two-dimensional interpretation of magnetotelluric soundings, *Geophys. J. Int.,* **133**(3), 585–606.

Berdichevsky, M.N., Kuznetsov, V.A. & Palshin, N.A., 2009. Analysis of magnetovariational response functions, *Izv. Phys. Sol. Earth,* **45**(3), 179–198.

Bijwaard, H., Spakman, W. & Engdahl, R.E., 1998. Closing the gap between regional and global travel time tomography, *J. geophys. Res.,* **103**(B12), 30 055–30 078.

Börner, R.-U., 2010. Numerical modelling in geo-electromagnetics: advances and challenges, *Surv. Geophys.,* **31,** 225–245.

Bostick, F.X., 1977. A simple almost exact method of MT analysis, in *Proceedings of Workshop on Electrical Methods in Geothermal Exploration,* U.S. Geological Survey, Snowbird, UT.

Brasse, H., Lezaeta, P., Rath, V., Schwalenberg, K., Soyer, W. & Haak, V., 2002. The Bolivian Altiplano conductivity anomaly, *J. geophys. Res.,* **107**(B5), 2096, EPM 3-1–EPM 3-14.

Cagniard, L., 1953. Basic theory of the magneto-telluric method of geophysical prospecting, *Geophysics,* **18,** 605–635.

Caldwell, T.G., Bibby, H.M. & Brown, C., 2004. The magnetotelluric phase tensor, *Geophys. J. Int.,* **158,** 457–469.

Cerv, V. & Pek, J., 1990. Modelling and analysis of electromagnetic fields in 3D inhomogeneous media, *Surv. Geophys.,* **11**(2–3), 205–229.

Chave, A.D. & Jones, A.G., Eds., 2012. *The Magnetotelluric Method: Theory and Practice,* Cambridge Univ. Press.

Chave, A.D. & Smith, J.T., 1994. On electric and magnetic galvanic distorion tensor decompositions, *J. geophys. Res. (Sol. Earth),* **99**(B3), 4669–4682.

Constable, S.C., Parker, R.L. & Constable, C.G., 1987. Occam's inversion: a practical algorithm for generating smooth models from electromagnetic sounding data, *Geophysics,* **52**(3), 289–300.

Eaton, D.W., Jones, A.G. & Ferguson, I.J., 2004. Lithospheric anisotropy structure inferred from collocated teleseismic and magnetotelluric observations: Great Slave Lake shear zone, northern Canada, *Geophys. Res. Lett.,* **31,** L19614, doi:10.1029/2004GL020939.

Garcia, X. & Jones, A.G., 2001. Decomposition of three-dimensional magnetotelluric data, in *Three-Dimensional Electromagnetics: Methods in Geochemistry and Geophysics,* Vol. 35, pp. 235–250, eds Zhdanov, M.S. & Wannamaker, P.E., Elsevier.

Garcia, X. & Jones, A.G., 2010. Internal structure of the western flank of the Cumbre Vieja volcano, La Palma, Canary Islands, from land magnetotelluric imaging, *J. geophys. Res.,* **115**(B7), 1–12.

Gibbons, W. & Moreno, T., Eds., 2002. *The Geology of Spain,* Geological Society.

Groom, R.W. & Bahr, K., 1992. Corrections for near surface effects: decomposition of the magnetotelluric impedance tensor and scaling corrections for regional resistivities—a tutorial, *Surv. Geophys.,* **13**(4-5), 341–379.

Groom, R.W. & Bailey, R.C., 1989. Decomposition of magnetotelluric impedance tensors in the presence of local three-dimensional galvanic distortion, *Journal of Geophysical Research (Solid Earth),* **94**(B2), 1913–1925.

Habashy, T., Groom, R. & Spies, B., 1993. Beyond the Born and Rytov approximations: a nonlinear approach to electromagnetic scattering, *J. geophys. Res.,* **98,** 1759–1776.

Heise, W. & Pous, J., 2001. Effects of anisotropy on the two-dimensional inversion procedure, *Geophys. J. Int.,* **147**(3), 610–621.

Jiracek, G.R., 1990. Near-surface and topographic distortions in electromagnetic induction, *Surv. Geophys.,* **11,** 163–203.

Jones, A., 1983. The problem of current channelling: a critical review, *Geophys. Surv.,* **6,** 79–122.

Jones, A.G., 1988. Static shift of magnetotelluric data and its removal in a sedimentary basin environment, *Geophysics,* **53**(7), 967–978.

Jones, A.G., 2006. Electromagnetic interrogation of the anisotropic Earth: looking into the Earth with polarized spectacles, *Phys. Earth planet. Inter.,* **158,** 281–291.

Jones, A.G., 2012. Distortion of magnetotelluric data: its identification and removal, in *The Magnetotelluric Method,* Chapter 6, pp. 219–302, eds Chave, A.D. & Jones, A.G., Cambridge Univ. Press.

Jones, A.G. & Groom, R.W., 1993. Strike angle determination from the magnetotelluric tensor in the presence of noise and local distortion: rotate at your peril! *Geophys. J. Int.,* **113,** 524–534.

Jones, A.G., Chave, A.D., Egbert, G., Auld, D. & Bahr, K., 1989. A comparison of techniques for magnetotelluric response function estimation, *J. geophys. Res. (Solid Earth),* **94**(10), 14 201–14 213.

Ledo, J., 2005. 2-D versus 3-D magnetotelluric data interpretation, *Surv. Geophys.,* **26,** 511–543.

Ledo, J., Queralt, P., Martí, A. & Jones, A., 2002. Two-dimensional interpretation of three-dimensional magnetotelluric data: an example of limitations and resolution, *Geophys. J. Int.,* **150,** 127–139.

Ledo, J., Jones, A.G., Siniscalchi, A., Campanyà, J., Kiyan, D., Romano, G., Rouai, M. & Team, T.M., 2011. Electrical signature of modern and ancient tectonic processes in the crust of the Atlas mountains of Morocco, *Phys. Earth planet. Inter.,* **185,** 82–88.

Marquis, G., Jones, A.G. & Hyndman, R.D., 1995. Coincident conductive and reflective middle and lower crust in southern British Columbia, *Geophys. J. Int.,* **120**(1), 111–131.

Martí, A., Queralt, P., Roca, E. & Ledo, J., 2009. Geodynamic implications for the formation of the Betic-rif Orogen from magnetotelluric studies, *J. geophys. Res.,* **114,** 1–14.

Matsuno, T. *et al.*, 2010. Upper mantle electrical resistivity structure beneath the central Mariana subduction system, *Geochem. Geophys. Geosyst.,* **11,** Q09003, doi:10.1029/2010GC003101.

McNeice, G.W. & Jones, A.G., 2001. Multisite, multifrequency tensor decomposition of magnetotelluric data, *Geophysics,* **66**(1), 158–173.

Miensopust, M.P., Jones, A.G., Muller, M.R., Garcia, X. & Evans, R.L., 2011. Lithospheric structures and precambrian terrane boundaries in northeastern Botswana revealed through magnetotelluric profiling as part of the southern African magnetotelluric experiment, *J. geophys. Res.,* **116**(B2), B02401, doi:10.1029/2010JB007740.

Muller, M.R. *et al.*, 2009. Lithospheric structure, evolution and diamond prospectivity of the Rehoboth terrane and western Kaapvaal craton, southern Africa: constraints from broadband magnetotellurics, *Lithos,* **112,** 93–105.

Niblett, E.R. & Sayn-Wittgenstein, C., 1960. Variation of electrical conductivity with depth by the magneto-telluric method, *Geophysics,* **25,** 998–1008.

Parker, R.L., 1980. The inverse problem of electromagnetic induction: existence and construction of solutions based on incomplete data, *J. geophys. Res.,* **85**(B8), 4421–4428.

Parker, R.L., 1983. The magnetotelluric inverse problem, *Geophys. Surv.,* **6,** 5–25.

Pek, J. & Santos, F.A., 2006. Magnetotelluric inversion for anisotropic conductivities in layered media, *Phys. Earth planet. Inter.,* **158**(2–4), 139–158.

Pek, J., Santos, F.A.M. & Li, Y., 2011. Magnetotelluric inversion for 2-D anisotropic conductivity, in *Proceedings of Geophysical Research Abstracts of the EGU General Assembly 2011,* Vol. 13, European Geophysical Union, Vienna, Austria, 2011 April 3–8. [Poster ID: EGU2011-2953-1]

Pellerin, L. & Hohmann, G.W., 1990. Transient electromagnetic inversion: a remedy for magnetotelluric static shifts, *Geophysics,* **55**(9), 1242–1250.

Poe, B.T., Romano, C., Nestola, F. & Smyth, J.R., 2010. Electrical conductivity anisotropy of dry and hydrous olivine at 8 GPa, *Phys. Earth planet. Inter.,* **181**(3–4), 103–111.

Pous, J., Muoz, G., Heise, W., Melgarejo, J.C. & Quesada, C., 2004. Electromagnetic imaging of Variscan crustal structures in SW Iberia: the role of interconnected graphite, *Earth planet. Sci. Lett.,* **217**(3–4), 435–450.

Rikitake, T., 1948. Notes on the electromagnetic induction within the Earth, in *Bulletin of the Earthquake Research Institute,* Chapter 1, pp. 1–9, Tokyo University's Earthquake Research Institute.

Rodi, W. & Mackie, R.L., 2001. Nonlinear conjugate gradients algorithm for 2-D magnetotelluric inversion, *Geophysics,* **66**(1), 174–187.

Rosell, O., Martí, A., Marcuello, À., Ledo, J., Queralt, P., Roca, E. & Campanyà, J., 2011. Deep electrical resistivity structure of the northern Gibraltar arc (western Mediterranean): evidence of lithospheric slab break-off, *TerraNova,* **23**(3), 179–186.

Schmoldt, J.-P., 2011. Multidimensional isotropic and anisotropic investigation of the Tajo Basin subsurface: a novel anisotropic inversion approach for subsurface cases with oblique geoelectric strike directions, *PhD thesis,* National University of Ireland, Galway, Ireland.

Schmoldt, J.-P. & Jones, A.G., 2013. On the electric conductivity structure and geology of the south-central Iberian Peninsula subsurface: Results of

a magnetotelluric investigation contrasted by seismic and thermal models, *Tectonics,* in press.

Schmucker, U., 1973. Regional induction studies: a review of methods and results, *Phys. Earth planet. Inter.,* **7**(3), 365–378.

Simpson, F. & Bahr, K., 2005. *Practical Magnetotellurics,* Cambridge Univ. Press.

Siripunvaraporn, W., Egbert, G. & Uyeshima, M., 2005. Interpretation of two-dimensional magnetotelluric profile data with three-dimensional inversion: synthetic examples, *Geophys. J. Int.,* **160,** 804–814.

Spitzer, K., 2006. Magnetotelluric static shift and direct current sensitivity, *Geophys. J. Int.,* **165**(1), 289–299.

Spratt, J.E., Jones, A.G., Jackson, V.A., Collins, L. & Avdeeva, A., 2009. Lithospheric geometry of the Wopmay orogen from a Slave craton to Bear Province magnetotelluric transect, *J. geophys. Res.,* **114**(B1), 1–18.

Tikhonov, A.N., 1950. The determination of electrical properties of the deep layers of the Earth's crust, *Dokl. Acad. Nauk. SSR,* **73,** 295–297 (in Russian).

Tikhonov, A.N., 1965. Mathematical basis of the theory of electromagnetic soundings, *USSR Comp. Math. Phys.,* **5,** 201–211.

Ting, S.C. & Hohmann, G.W., 1981. Integral equation modeling of three-dimensional magnetotelluric response, *Geophysics,* **46**(2), 182–197.

Tournerie, B. & Chouteau, M., 2005. Three-dimensional magnetotelluric survey to image structure and stratigraphy of a sedimentary basin in Hungary, *Phys. Earth planet. Inter.,* **150,** 197–162.

Utada, H. & Munekane, H., 2000. On galvanic distortion of regional three-dimensional magnetotelluric impedances, *Geophys. J. Int.,* **140**(2), 385–398.

Villaseñor, A., Spakman, W. & Engdahl, E., 2003. Influence of regional travel times in global tomographic models, in *Proceedings of EGS-AGU-EUG Joint Assembly,* Vol. **5,** pp. EAE03–A–08614, Geophysical Research Abstracts, Nice, France, 2003 April 6–11.

Villaseñor, A., Yang, Y., Ritzwoller, M.H. & Gallart, J., 2007. Ambient noise surface wave tomography of the Iberian Peninsula: implications for shallow seismic structure, *Geophys. Res. Lett.,* **34,** L11304, doi:10.1029/2007GL030164.

Vozoff, K., 1986. *Magnetotelluric Methods,* Vol. 5, Society of Exploration Geophysics (reprint).

Vozoff, K., 1991. The magnetotelluric method, in *Electromagnetic Methods in Applied Geophysics: Theory,* Vol. 2, pp. 641–712, Society of Exploration Geophysics.

Wannamaker, P.E., Hohmann, G.W. & Filipo, S.W.A., 1984. Electromagnetic modeling of three-dimensional bodies in layered earths using integral equations, *Geophysics,* **49,** 60–74.

Wannamaker, P.E. *et al.*, 2009. Fluid and deformation regime of an advancing subduction system at Marlborough, New Zealand, *Nature,* **460**(7256), 733–736.

Weaver, J.T., Agarwal, A.K. & Lilley, F. E.M., 2000. Characterization of the magnetotelluric tensor in terms of its invariants, *Geophys. J. Int.,* **141,** 321–336. [WALDIM basis paper]

Weidelt, P., 1972. The inverse problem of geomagnetic induction, *Zeitschrift für Geophysik,* **8**(2), 257–290.

WinGLink, 2005. *WinGLink User's Guide,* 2nd edn, WesternGeco. [Formerly Geosystem Srl.]

Wu, X., Ferguson, I.J. & Jones, A.G., 2005. Geoelectric structure of the Proterozoic Wopmay Orogen and adjacent terranes, Northwest Territories, *Can. J. Earth Sci.,* **981,** 955–981.

A P P E N D I X   A

A1 Anisotropic 1-D inversion

A1.1 Inversion approach

The use of anisotropic inversion to recover the 3-D model is motivated by the fact that 2-D structures can be imaged by an anisotropic 1-D region and vice versa (e.g. Heise & Pous 2001; Pek & Santos 2006). The principle of using anisotropy to image macroscale 2-D

structures can be best illustrated using basic MT relations, which are recapped here briefly; for a broader discussion of MT relations the interested reader is referred to the standard literature (e.g. Schmucker 1973; Vozoff 1991; Berdichevsky 1999; Simpson & Bahr 2005; Becken *et al.* 2008; Berdichevsky *et al.* 2009; Chave & Jones 2012) as well as the review papers on MTNet and references therein.

A significant degree of anisotropy in an otherwise 1-D subsurface can cause decoupling of the off-diagonal impedance tensor elements (eq. 2) that is similar to a 2-D subsurface case (*cf.* eq. 7) with respective directions of the coordinate system. In such a case, the TE and TM modes of the 2-D subsurface case can be imaged by the relatively conductive and resistive anisotropy direction:

$$\mathbf{Z}_{2D} = \begin{pmatrix} 0 & Z_{xy}(T) \\ Z_{yx}(T) & 0 \end{pmatrix} \qquad (A1)$$

$$\Leftrightarrow \begin{pmatrix} 0 & Z_{xy}^{ani}(T) \\ Z_{yx}^{ani}(T) & 0 \end{pmatrix} = \mathbf{Z}_{1D}^{ani}, \qquad (A2)$$

where Z_{xy}^{ani} and Z_{yx}^{ani} are special forms of the 1-D impedance tensor elements given in eq.(5) that comprise the electric conductivity of the subsurface for the respective direction. Certainly, values of the

two 2-D subsurface modes, TE and TM (i.e. Z_{xy} and Z_{yx}), differ between conductive and resistive side of the interface and vary with (inductive) distance from the interface. It will be shown that such behaviour at a vertical interface can be accounted for through the corresponding selection of electric anisotropy direction and a changing magnitude of anisotropy for the respective stations and periods.

A1.2 Inversion process

In this study, anisotropic 1-D inversion is carried out using the `ai1d` algorithm by Pek & Santos (2006). The `ai1d` algorithm yields impedance values in terms of minimum resistivity ρ_{min}, maximum resistivity ρ_{max} and 'anisotropic direction' for different depths at each station. Anisotropic direction denotes the angle between ρ_{max} and the *x*-axis; for this anisotropic 1-D study, the latter is oriented towards true north. Inversion time of the anisotropic 1-D approach is marginal, in the order of a few minutes on a normal desktop computer.

A1.3 Inversion results

In here, inversion results are shown for the same stations used in the isotropic 2-D inversion, that is, stations syn001–syn020 (see
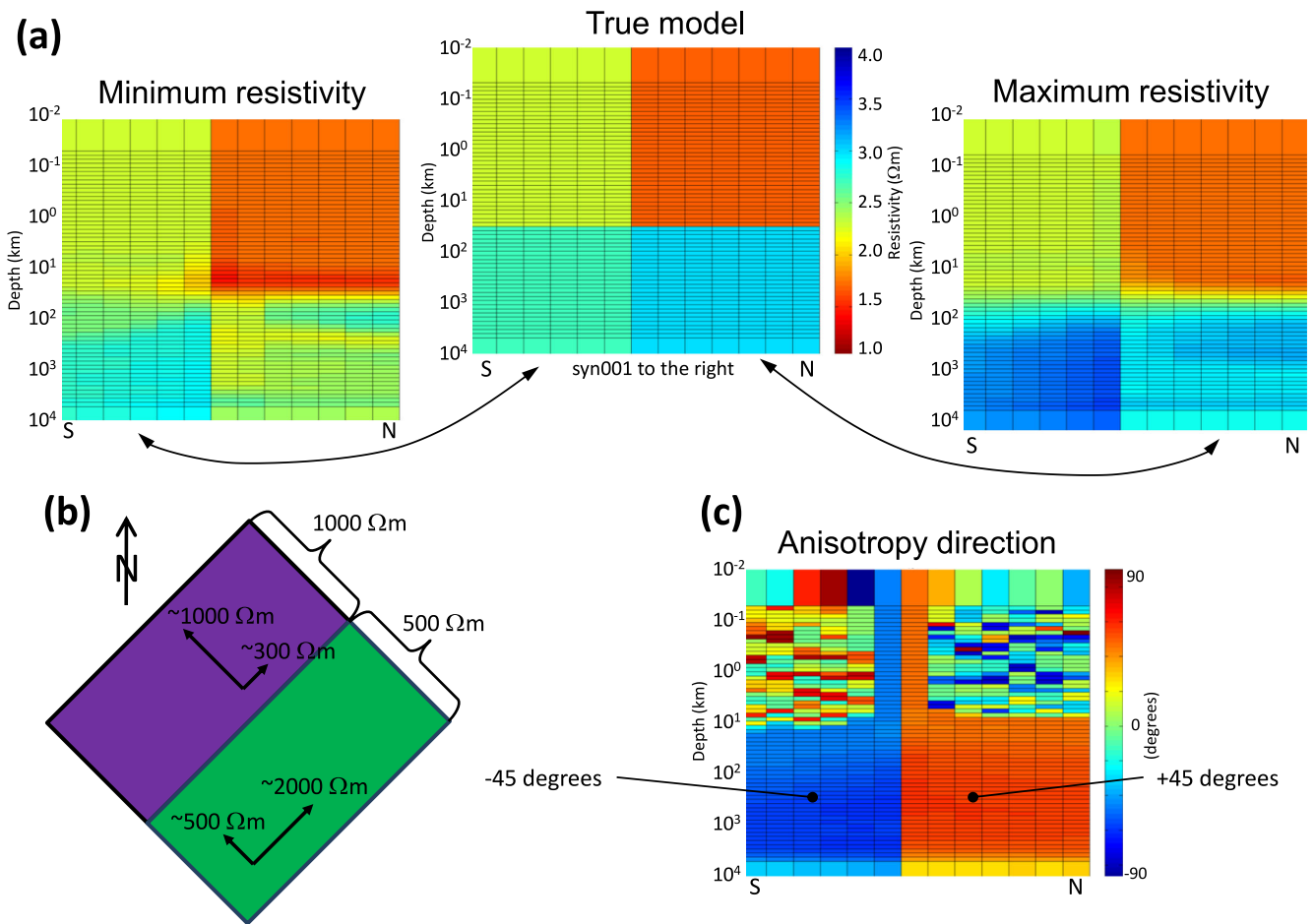

Figure A1. 1-D anisotropic inversion of the 3-D subsurface model (Fig. 1) using the `ai1d` algorithm by Pek & Santos (2006) showing that (a) the true model can be reproduced from a combination of derived minimum and maximum inversion models. The strike direction of the true model is −45° (N45W) at crustal and +45° (N45E) at mantle depth. Values and direction of minimum and maximum resistivity obtained through 1-D anisotropic inversion of the 3-D model are indicated in plots (b) and (c); the former only refers to values at mantle depths. Note that the strike direction for the crust are insignificant since the degree of anisotropy is negligible (*cf.* Fig. A2).

Fig. 2 in the main text). Results of the anisotropic 1-D inversion for each station are plotted side-by-side to yield pseudo-2-D subsurface models for ρ_{min} and ρ_{max}, thereby facilitating comparison of results from different inversion approaches. Crustal-range values of ρ_{min} and ρ_{max} (depths ≤ 30 km in left- and right-hand plots of Fig. A1) are similar to each other (hence isotropic) and to the true subsurface model (uppermost plot in Fig. A1). Mantle structures, on the other hand, are significantly different. The south (left-hand side) mantle region of the ρ_{min} model is similar to the true model, whereas the mantle region to the north (right-hand side) is clearly different. For the ρ_{max} model the opposite case occurs; the mantle region to the right is similar to the true model, whereas the mantle region to the left is significantly different (indicated by arrows in Fig. A1). The magnitude of anisotropy is given in terms of the difference between ρ_{min} and ρ_{max} at crustal and mantle depths (Fig. A2). Whereas at crustal depth the ρ_{max}/ρ_{min} quotient is approximately one, values between three and eight are observed for the mantle region. The region of maximum anisotropy magnitude is located at a depth

between 100 and 500 km in the resistive region of the mantle [in the right-hand side of plot (b) in Fig. A2].

Analysis of the anisotropic strike direction shown at the bottom of Fig. A1 reveals that for the region to the right the anisotropic strike is parallel to the geoelectric 2-D strike at mantle depth, that is, $+45°$ or N45E, whereas for the region to left the anisotropic strike direction is orthogonal to it. Sorting the resistivity values of the models according to their orientation yields models of resistivity parallel to the 2-D strike of the synthetic model at mantle depth ($\rho_\parallel$) and orthogonal to it ($\rho_\perp$). Comparison with the true models shows that the $\rho_\parallel$ model exhibits an electric resistivity distribution similar to the true model, whereas the $\rho_\perp$ model underestimates the resistivity in the relatively resistive region and overestimates the resistivity on the relatively conductive side (*cf.* Fig. A3).

The difference between $\rho_\parallel$ and the true model is mostly confined to a small area at the crust–mantle boundary to the northern end of the profile (*cf.* Figs A3 and A4). The misfit coincides with the transition from 50 to 1000 Ωm in the true model and it is concluded
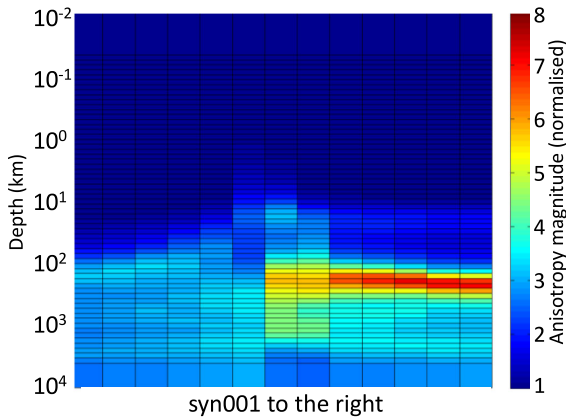

Figure A2. Magnitude of anisotropy for the 1-D inversion calculated from the $\rho_{max} - \rho_{min}$ quotient exhibiting a rather isotropic crust and a mantle with an anisotropic magnitude between 1 and 8.
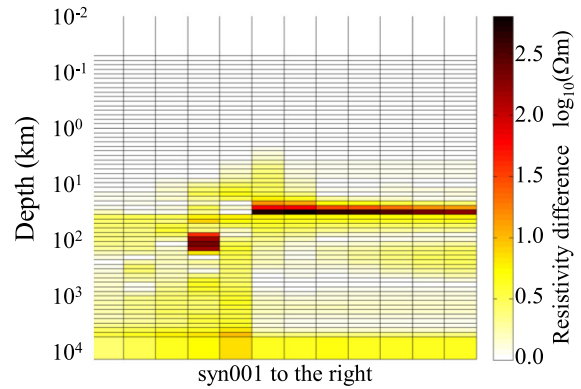
Figure A4. (a) Comparison of $\rho_\parallel$ and $\rho_\perp$ model with the true model, demonstrating good agreement of the $\rho_\parallel$ model. (b) Relative difference between the model with resistivity values parallel to the 2-D strike ($\rho_\parallel$) and the true model.
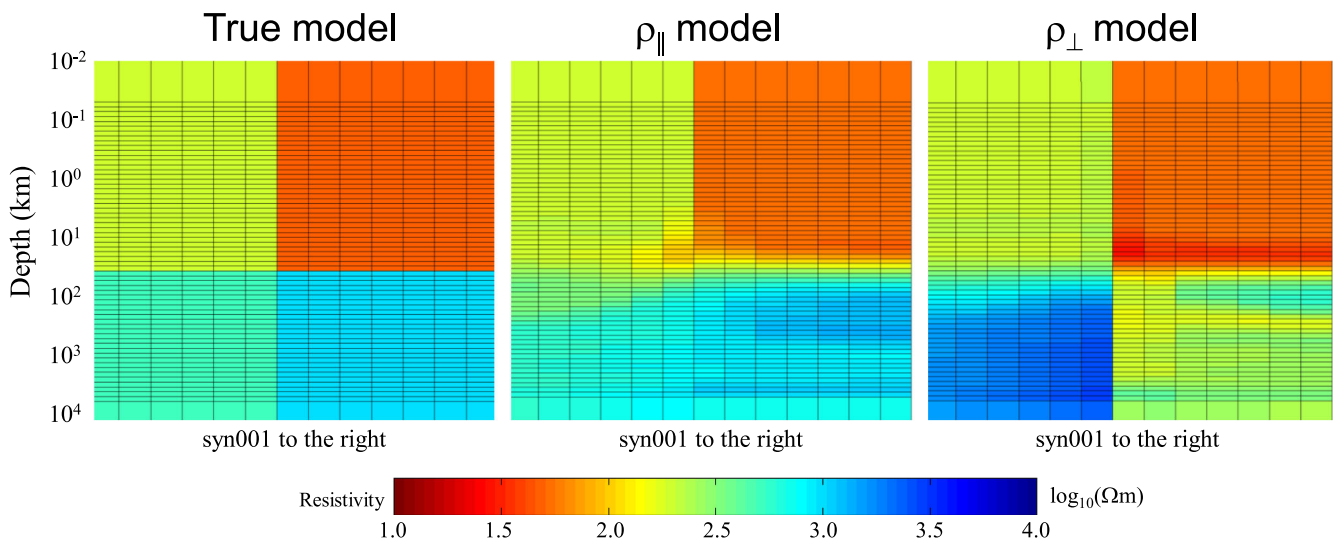

Figure A3. (a) Comparison of $\rho_\parallel$ and $\rho_\perp$ model with the true model, demonstrating good agreement of the $\rho_\parallel$ model. (b) Relative difference between the model with resistivity values parallel to the 2-D strike ($\rho_\parallel$) and the true model.

that the discrepancy originates from smoothing regularizations of the inversion process, meaning that the 1-D anisotropic inversion yields an adequate reproduction of the synthetic model for the major part of the mantle. However, the 3-D subsurface model used in this study comprises a considerably simple electric conductivity structure, and 1-D anisotropic inversion is likely to fail for more complex models, for example, a model containing dipping structures. Results of the ai1d algorithm may rather be used as a first approach to the subsurface structures and to construct an elaborate starting model for subsequent 2-D or even 3-D inversions.